

Controlled flight of a microrobot powered by soft artificial muscles

<https://doi.org/10.1038/s41586-019-1737-7>

Received: 21 April 2019

Accepted: 18 September 2019

Published online: 4 November 2019

Yufeng Chen^{1,2,3*}, Huichan Zhao⁴, Jie Mao^{1,5}, Pakpong Chirarattananon⁶, E. Farrell Helbling^{1,2}, Nak-seung Patrick Hyun^{1,2}, David R. Clarke¹ & Robert J. Wood^{1,2*}

Flying insects capable of navigating in highly cluttered natural environments can withstand in-flight collisions because of the combination of their low inertia¹ and the resilience of their wings², exoskeletons¹ and muscles. Current insect-scale (less than ten centimetres long and weighing less than five grams) aerial robots^{3–6} use rigid microscale actuators, which are typically fragile under external impact. Biomimetic artificial muscles^{7–10} that are capable of large deformation offer a promising alternative for actuation because they can endure the stresses caused by such impacts. However, existing soft actuators^{11–13} have not yet demonstrated sufficient power density to achieve lift-off, and their actuation nonlinearity and limited bandwidth create further challenges for achieving closed-loop (driven by an input control signal that is adjusted based on sensory feedback) flight control. Here we develop heavier-than-air aerial robots powered by soft artificial muscles that demonstrate open-loop (driven by a predetermined signal without feedback), passively stable (upright during flight) ascending flight as well as closed-loop, hovering flight. The robots are driven by multi-layered dielectric elastomer actuators that weigh 100 milligrams each and have a resonance frequency of 500 hertz and power density of 600 watts per kilogram. To increase the mechanical power output of the actuator and to demonstrate flight control, we present ways to overcome challenges unique to soft actuators, such as nonlinear transduction and dynamic buckling. These robots can sense and withstand collisions with surrounding obstacles and can recover from in-flight collisions by exploiting material robustness and vehicle passive stability. We also fly two micro-aerial vehicles simultaneously in a cluttered environment. They collide with the wall and each other without suffering damage. These robots rely on offboard amplifiers and an external motion-capture system to provide power to the dielectric elastomer actuators and to control their flight. Our work demonstrates how soft actuators can achieve sufficient power density and bandwidth to enable controlled flight, illustrating the potential of developing next-generation agile soft robots.

Soft robotics^{14–16} is an emerging field that aims to develop versatile systems that can safely interact with humans and manipulate delicate objects in unstructured environments. A major challenge in building soft-actuated mobile robots involves developing muscle-like actuators that have high energy density, bandwidth, robustness and lifetime. Previous studies have described soft actuators that can be actuated chemically¹⁷, pneumatically^{18,19}, hydraulically²⁰, thermally^{21,22} or electrically^{7,23}. Among these soft transducers, dielectric elastomer actuators (DEAs) have shown a combination of muscle-like energy density and bandwidth⁸, enabling the development of biomimetic robots capable of terrestrial^{11,24,25} and aquatic locomotion^{26,27}. However, although there is growing interest in developing heavier-than-air, soft-actuated aerial

robots, existing soft robots^{11–13} have been unable to achieve lift-off owing to limited actuator power density ($<200 \text{ W kg}^{-1}$), limited bandwidth ($<20 \text{ Hz}$) and the difficulties of integration with rigid robotic structures such as transmission and wings.

To enable controlled hovering flight of a soft-actuated robot, we identify and address two major challenges: developing a soft actuator with sufficient power density ($>200 \text{ W kg}^{-1}$) and designing driving and control strategies to account for actuation nonlinearity (see Methods section ‘Conceptual design of a DEA-powered aerial robot’ and Extended Data Table 1 for details on vehicle design and DEA performance requirements). First, we develop a multi-layered, compact DEA that has a power density of 600 W kg^{-1} without requiring pre-strain.

¹John A. Paulson School of Engineering and Applied Sciences, Harvard University, Cambridge, MA, USA. ²Wyss Institute for Biologically Inspired Engineering, Harvard University, Cambridge, MA, USA. ³Research Laboratory of Electronics, Massachusetts Institute of Technology, Cambridge, MA, USA. ⁴Department of Mechanical Engineering, Tsinghua University, Beijing, China.

⁵College of Chemical and Biological Engineering, Zhejiang University, Hangzhou, China. ⁶Department of Biomedical Engineering, City University of Hong Kong, Hong Kong, China. *e-mail: yufengc@mit.edu; rjwood@eecs.harvard.edu

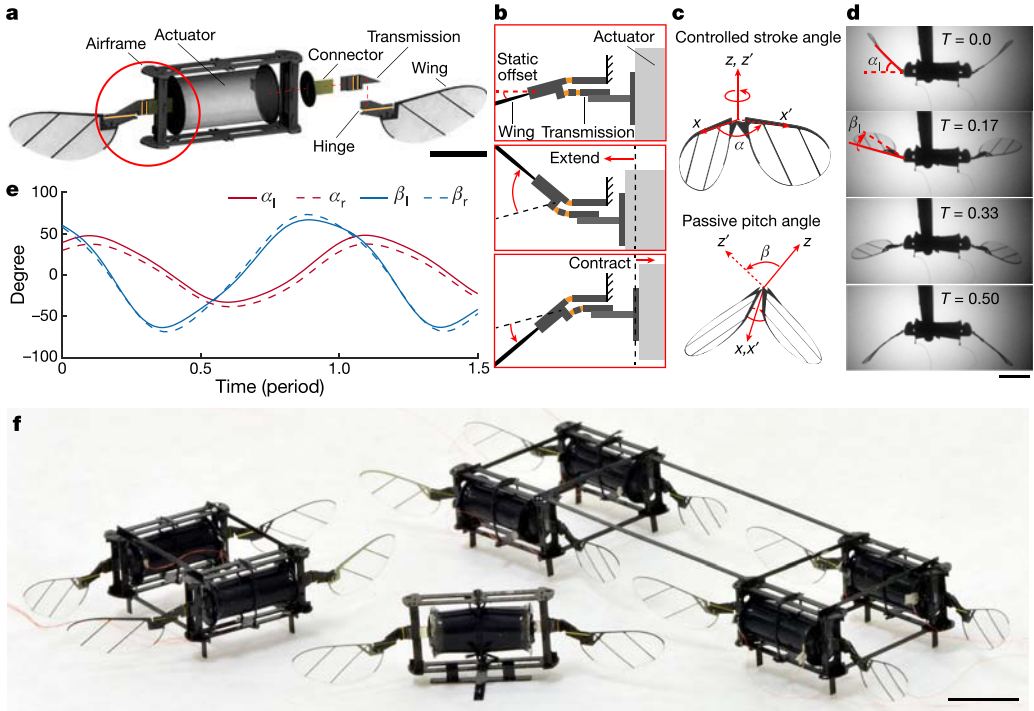


Fig. 1 | Robot design and flapping wing kinematics. **a**, A computer aided design (CAD) model of a 155-mg flapping-wing robot driven by a DEA. The exploded view of the robot's right half shows the actuator, connector, four-bar transmission, wing and wing hinge. The circled region of the robot's left transmission is magnified in **b**. **b**, Enlarged top view of the robot's actuator-transmission-wing assembly. The DEA is pre-strained by 2% when it is attached to the robot's transmissions, which induces a static stroke angle bias of approximately 15° (first panel). The DEA extension and contraction (second and third panels, respectively) are translated into the rotational wing stroke motion. **c**, Illustrations of the actively controlled wing stroke (α) motion (first

panel) and the passive wing pitch (β) motion (second panel). **d**, An image sequence of the flapping wing motion operated at 280 Hz. The time T is normalized to a flapping period (that is, 0.5 is half a period). The left wing stroke rotation (α_l) induces passive wing pitch rotation (β_l). **e**, Tracked flapping wing kinematics that correspond to the experiment shown in **d**. The wing stroke (red) amplitudes of the left (solid line) and the right (dotted line) wings are 42° and 41°, respectively. The wing pitch (blue) amplitudes of the left (solid line) and the right (dotted line) wings are 57° and 61°, respectively. **f**, Image of flapping-wing microrobots driven by a single actuator, two actuators, and four actuators. Scale bars in **a**, **d** and **f** represent 5 mm.

Second, we integrate the DEA into a lightweight, flapping-wing mechanism and utilize system resonance to remove higher harmonics induced by the nonlinear transduction. In combination, we design a 155-mg flapping-wing module that can be assembled into several configurations. Using these modules, we are able to construct vehicles that not only demonstrate passively stable ascending flight but also controlled hovering flight.

Our robot is driven by a multi-layered DEA rolled into a cylindrical shell to generate linear actuation (see Methods section 'Fabrication of robot components' and Extended Data Figs. 1 and 2 for details on DEA fabrication). The DEA is mounted in a light-weight airframe (Fig. 1a), with the two ends of the DEA attached to planar four-bar transmissions. This design allows one DEA to simultaneously actuate two wings in a manner analogous to what the indirect flight muscles do in neopteran flying insects²⁸. By using the planar four-bar transmissions, the DEA's axial extension and contraction are converted into the wing's rotational stroke motion (Fig. 1b). In quasi-static operation, the actuation is unidirectional because DEA strain is proportional to the square of the applied electric field. In dynamic operation, the DEA extends and contracts as a result of its intrinsic inertia and stiffness, yet its elongation amplitude is larger than the retraction amplitude. To ensure the mean wing stroke (α) motion is symmetric with respect to the robot body, the resting wing stroke plane is offset by approximately 15° (Fig. 1b) during robot assembly. The DEA is pre-strained by 2% when it is attached to the robot transmissions, and this pre-strain loads the elastic four-bar transmissions to introduce the wing stroke bias. This small pre-strain does not noticeably change the DEA performance, and the design is advantageous compared to artificial flight muscles with a

large pre-strain¹¹ (>100%) because it does not require a rigid and heavy supporting structure. In this way, the robot wing stroke (α) motion is fully controlled by the actuator, whereas the wing pitch (β) rotation is passively mediated by the compliant wing hinge (Fig. 1c). Figure 1d and Supplementary Video 1 show a half flapping period actuated at 280 Hz. The tracked wing stroke and pitch motion for the same experiment are shown in Fig. 1e. On the basis of an aerodynamic model developed in a previous study²⁹, we estimate that this flapping motion will generate a net lift force of approximately 1.8 mN, corresponding to 1.2 times the robot weight. This modular robot can be assembled into several configurations to demonstrate different flight capabilities. For instance, Fig. 1f shows micro-aerial vehicles (MAVs) driven by one (centre panel), two (left panel) and four DEAs (right panel). These vehicles exhibit open loop lift-off (one DEA), stable ascending flight (two DEAs) and hovering flight through feedback control (four DEAs), respectively.

To achieve flight of a soft-actuated robot, the DEA must have sufficient power density and the robot transmissions and wings must be designed around the actuator's output force, displacement and bandwidth. In contrast to previous studies¹¹ that developed pre-strained acrylic DEAs to achieve large deformation (>30%) and high energy density (>4 J kg⁻¹) but low bandwidth (<30 Hz), we use a silicone elastomer as the dielectric material for the flight muscles to achieve higher bandwidth (>400 Hz), combined with moderate strain (10–15%) and energy density (1.13 J kg⁻¹). For driving frequencies lower than 600 Hz, our DEA's blocked force (Fig. 2a) is independent of frequency because its electrical properties are tuned to have a small RC time constant of 0.18 ms. The DEA's free displacement (Fig. 2b) peaks at 15% strain when it is driven at 500 Hz. The free displacement amplitude includes the

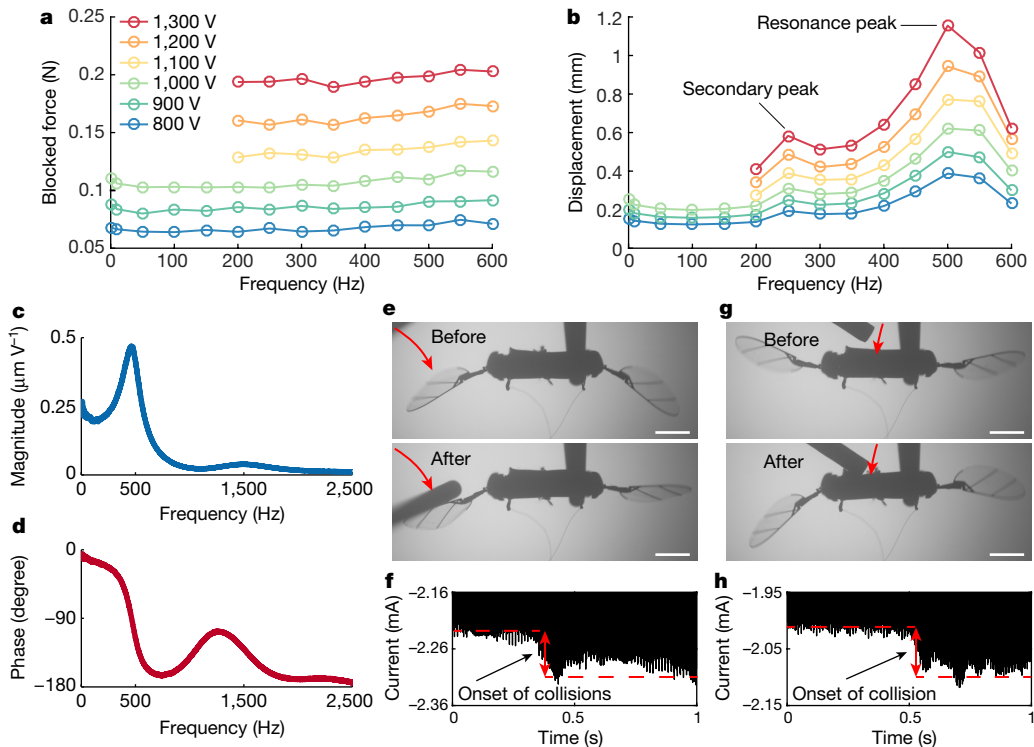


Fig. 2 | DEA performance, robustness, and collision sensing. **a, b**, Measured DEA blocked force (**a**) and free displacement (**b**) as functions of operating frequency and voltage amplitude. In **a** and **b**, there are no experiments conducted for the cases combining low frequency (<200 Hz) and high voltage (>1,000 V) because the elastomer cannot endure a large electric field at low frequencies. **c, d**, Frequency response of the DEA free displacement under an input voltage of 600 V. **c** and **d** show the magnitude and phase of the frequency

response, respectively. **e**, A flapping wing repeatedly collides with an obstacle when the DEA is operated at 320 Hz and 1,350 V. **f**, Measured DEA current as a function of time. The jump in the DEA current indicates the onset of the wing–obstacle collisions. **g**, A rigid object presses down on the DEA that is operating at 320 Hz and 1,300 V. **h**, The jump in the measured DEA current indicates the time that the object makes contact with the DEA. Scale bars in **e** and **g** are 5 mm.

contribution from the first and higher-order harmonics in response to a sinusoidal driving signal. We observe a secondary peak of free displacement (Fig. 2b) when the driving frequency is 250 Hz, owing to exciting the second-order harmonic that is near the resonant frequency (500 Hz). Our robot design utilizes the first harmonic to drive the flapping-wing motion. By computing the fast Fourier transform (FFT) of the DEA's response to white noise, we quantify the magnitude (Fig. 2c) and phase (Fig. 2d) of the linear part of its response. When operated under the takeoff conditions (300 Hz, 1,300 V), the DEA has a power density of 300 W kg^{-1} and a lifetime of over 600,000 cycles (see Methods section ‘DEA performance characterization’ for details on the actuator characterization).

Powering MAVs using soft actuators has an advantage over state-of-the-art flapping wing microrobots (<10 cm, <5 g) driven by rigid actuators such as piezoelectric bimorphs³ and electromagnetic motors⁵. Although microrobotic components—such as the airframe, transmissions and wings—are robust to collisions (because inertial contributions diminish at the millimetre scale), rigid micro-actuators are fragile—particularly the piezoceramic actuators (fracture strength and failure strain are 120 MPa and 0.3%, respectively) used in many similarly sized devices^{3,4}. In contrast, this DEA-driven microrobot is robust to collisions. For instance, when one wing collides with an obstacle (Fig. 2e and Supplementary Video 2), the impact is absorbed by the DEA because of its high compliance and resilience. In addition, the DEA can detect collisions (Fig. 2f) through concomitant actuation and sensing under similar principles to that of electromagnetic motors³⁰ and piezoelectric actuators³¹. Similarly, if an obstacle directly hits the DEA during its actuation (Fig. 2g and Supplementary Video 2), the DEA deformation can also be detected by monitoring the current (Fig. 2h). These experiments show that DEA is not only robust to collisions, but is also

capable of sensing collisions with the environment (see Supplementary Information section S1 and Extended Data Fig. 3 for more experimental results on collision sensing). Despite these favourable properties (such as robustness and self-sensing), DEAs present challenges for achieving flight owing to their inherent nonlinearity. The strain in a DEA is proportional to the square of the applied electric field⁷. Consequently, a sinusoidal driving signal does not result in symmetric up stroke and down stroke motion (Fig. 3a and Supplementary Video 3) because of the influence of higher-order harmonics (see Supplementary Information section S2 and Extended Data Fig. 4 for details on nonlinear actuation and higher harmonics). For example, when operated at 100 Hz, the wing down stroke exhibits a slow reversal from $T=0.5$ to $T=0.7$ (Fig. 3a and Supplementary Video 3). According to a previous aerodynamic study²⁹, this slow wing reversal can result in a substantial reduction in lift force. To mitigate the up stroke and down stroke asymmetry, we drive the DEA near the resonant frequency of the DEA–transmission–wing system to amplify the fundamental harmonic and attenuate higher harmonics. This asymmetry is substantially reduced when the DEA is driven at a frequency that is higher than half its resonance. Compared to flapping motion at 1 Hz or 100 Hz, the slow wing reversal is negligible when the driving frequency increases to 280 Hz (Fig. 3b and Supplementary Video 3).

In addition to exhibiting nonlinear transduction, the DEA can undergo dynamic buckling that substantially affects flapping motion and reduces the lift force. When operated near the system resonance, the DEA experiences a large compressive load that is due to the drag force from the robot wing. This normal load causes the DEA to buckle along a direction perpendicular to its actuation axis. The actuator returns to its nominal configuration as this compressive load is reduced during wing reversal. In the next flapping period, the DEA buckles in the

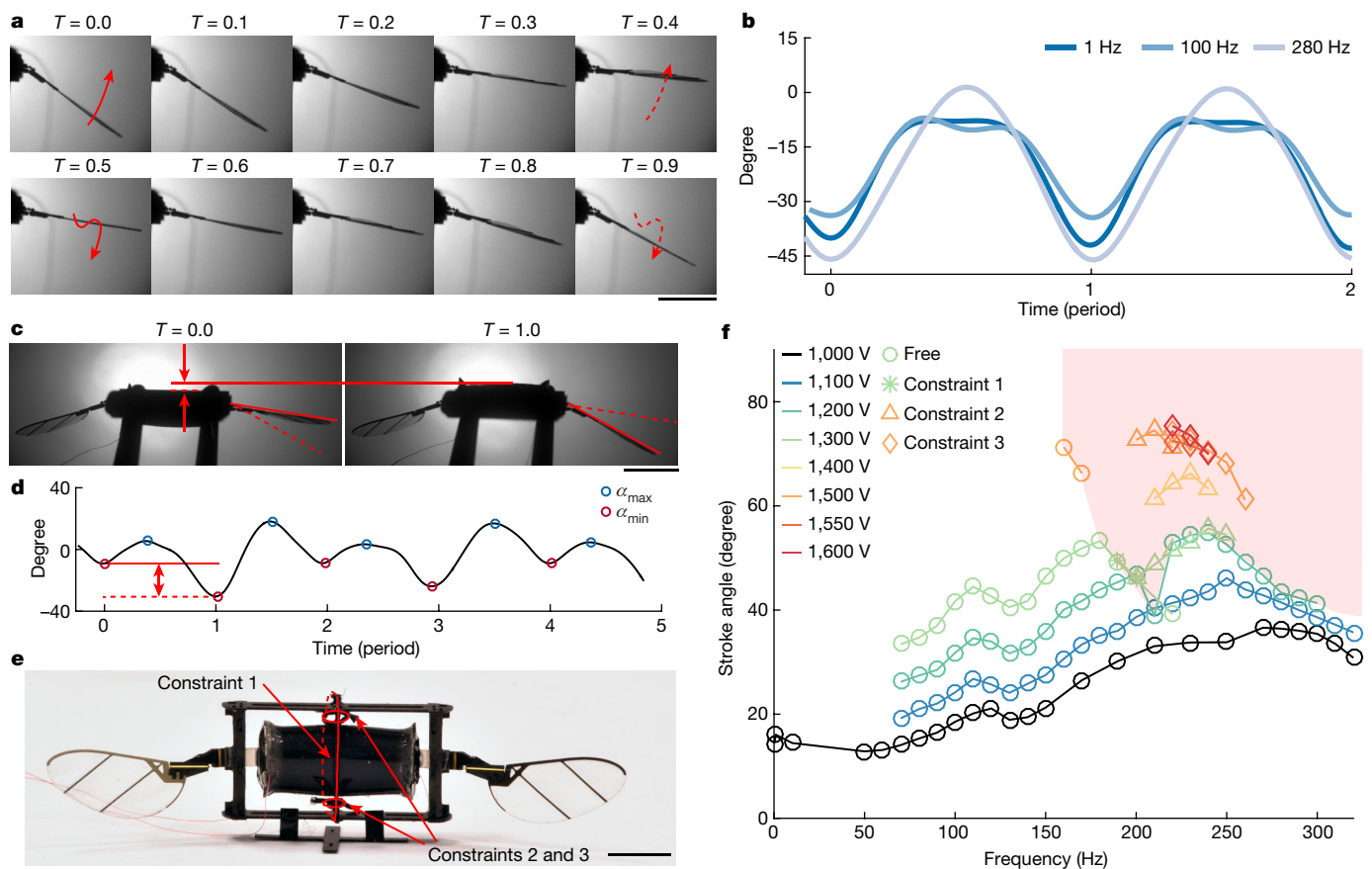


Fig. 3 | DEA nonlinearity and dynamic buckling. **a**, Image sequence of the robot flapping motion at 100 Hz for one flapping period. The up stroke and down stroke are asymmetric. **b**, Tracked wing stroke motion at 1 Hz, 100 Hz and 280 Hz. The wing stroke motion is asymmetric at low flapping frequencies. The nonlinear high-frequency modes are reduced by post-resonant inertial effects. **c**, Images that illustrate the DEA dynamic buckling. The red lines indicate that the DEA buckles and the wing stroke amplitude reduces. **d**, Tracked wing stroke

motion that corresponds to the experiment shown in **c**. The wing stroke amplitude reduces and the flapping period halves. **e**, Three pieces of thread circumferentially constrain the DEA to the robot airframe to eliminate out-of-plane motion and inhibit dynamic buckling. **f**, Stroke amplitude as a function of driving voltage and frequency. The red-shaded region represents the stroke amplitudes and flapping frequencies that are unachievable without constraining the DEA. Scale bars in **a**, **c** and **e** represent 5 mm.

opposite direction owing to the momentum of the restoring motion. Dynamic buckling substantially reduces the wing stroke amplitude (Fig. 3c, d and Supplementary Video 3), and it occurs at half the flapping frequency (Fig. 3d and Supplementary Video 3). Further, the large DEA deformation causes excessive electrode self-clearing and substantially reduces DEA performance and lifetime. Dynamic buckling can be inhibited by using circumferential constraints (in this case, strings) to limit the DEA's off-axis motion at its mid-plane (Fig. 3e). Figure 3f shows the left wing's stroke amplitude as a function of driving frequency and voltage. The kinks of the green lines indicate stroke amplitude reduction due to dynamic buckling. Constraining the DEA's off-axis motion enables higher driving voltages and frequencies, which correspond to higher wing stroke amplitudes. The red-shaded region indicates operating conditions that are inaccessible without constraining the DEA. Adding constraints increases the wing stroke peak-to-peak amplitude by approximately 25°, leading to a 1.6-fold increase in lift force.

Addressing the challenges of nonlinear actuation enables flight demonstrations of the DEA-driven, flapping-wing microrobots. All flight demonstrations are unconstrained, but the robots carry a thin tether for offboard power supply and control. Driven by a single DEA, the 155-mg robot demonstrates open-loop lift-off. The net lift generated by this MAV is approximately 1.8 mN, and it reaches a maximum height of 1.5 cm in 90 ms (Fig. 4a and Supplementary Video 4). To mitigate aerodynamic torque imbalances caused by fabrication and assembly imprecision, a carbon fibre rod with a point mass is attached to the

robot's airframe to adjust its centre of mass position. However, without attitude (orientation of flying vehicle) and position control authority, this intrinsically unstable robot flips over within 110 ms of lift-off.

To demonstrate stable ascending flight, we build a two-actuator, four-winged robot (Fig. 1e) that uses precession around the body z-axis to achieve passive stability. We bias the resting wing's pitch angle during robot assembly to induce a net yaw torque around the robot's body z-axis. The body z-component of the angular momentum induced by precession rejects the robot's pitch and roll torque imbalances. In an open-loop takeoff experiment, we demonstrate that the robot reaches a height of 23.5 cm within 0.83 s of open-loop takeoff (Fig. 4b and Supplementary Video 5). We also construct a dynamical model and use numerical simulation to confirm the experimental observation on passive upright stability. Our simulation (Fig. 4c) shows that the robot ascends 22.7 cm in 0.83 s with a yaw rate of 17.2 revolutions per second. This passive stability property further enables us to operate more than one robot in a confined space without the need of motion tracking and feedback control. We demonstrate simultaneous takeoff flights of two robots (Supplementary Video 6) and show that they are robust against collisions with the surroundings and each other. In addition, passive stability and collision robustness can provide the ability to recover from in-flight collisions or disturbances. Figure 4d and Supplementary Video 6 show a collision recovery flight in which the robot takes off from the centre of a cylindrical shell, collides with the shell wall during its ascent, and continues to fly upward after the collision. However,

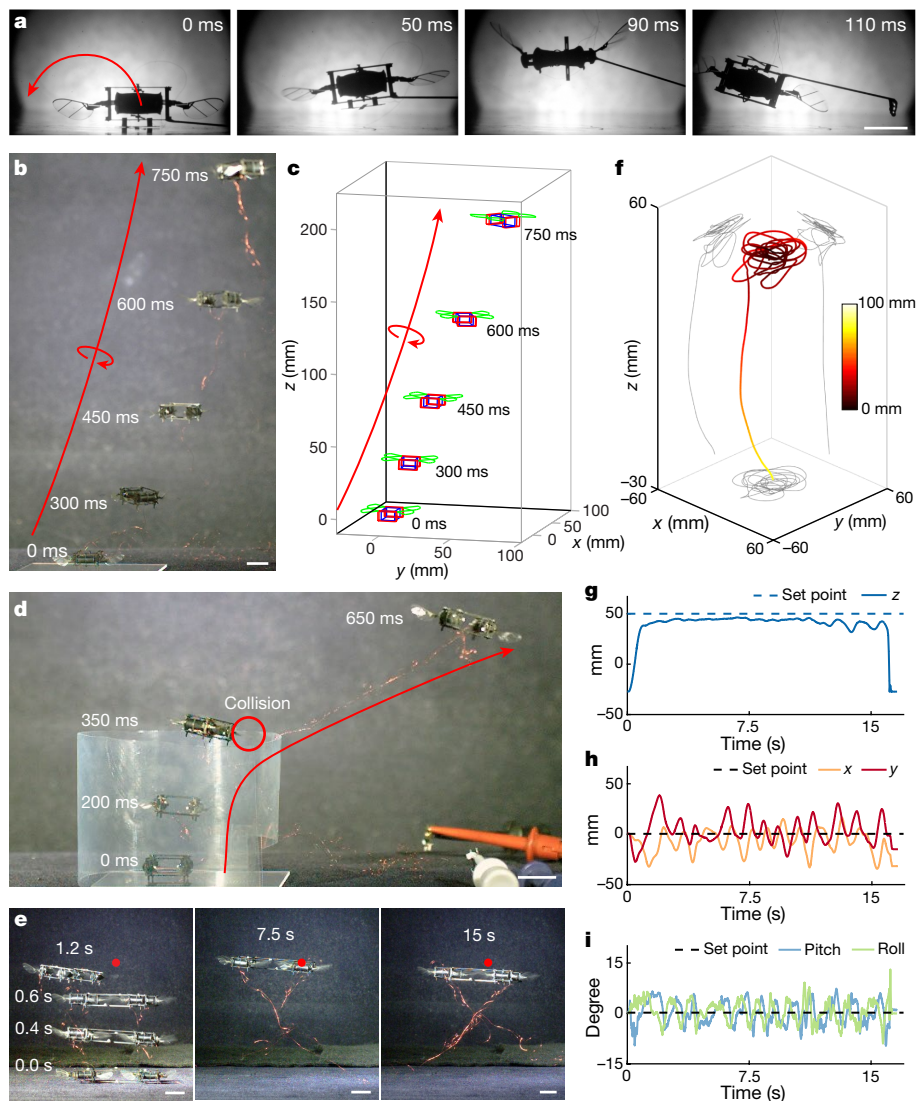


Fig. 4 | Robot flight demonstrations. **a**, Unstable lift-off of a 155-mg robot driven by one DEA. The robot reaches a height of 1.5 cm and then flips upside down owing to unstable body pitch rotation. **b, c**, Passively stable ascending flight of a 320-mg robot driven by two DEAs. Both the experiment (**b**) and the dynamical simulation (**c**) show that the robot reaches approximately 23 cm within 0.75 s of open-loop takeoff. The simulation shows that the robot precesses at a yaw rate of 17.2 revolutions per second. **d**, The 320-mg robot

remains passively upright stable after colliding with an obstacle and continues to fly upward. **e**, Composite images of a 16-s controlled hovering flight that is demonstrated by a 660-mg robot driven by four DEAs. **f**, The tracked flight trajectory corresponding to the experiment in **e**. The colour scale denotes the distance between the robot position and the set point (the desired hovering position). **g–i**, Robot altitude (**g**), *x* and *y* positions (**h**), and attitude (**i**) as functions of time. Scale bars in **a, b, d** and **e** are 1 cm.

passive in-flight collision recovery is a probabilistic event that depends on the robot's flight speed and the collision impact. Without any robot attitude sensing and feedback control, the robot may be destabilized after experiencing one or multiple collisions (see Supplementary Information section S3, Extended Data Figs. 5–9, and Extended Data Table 2 for a detailed discussion on passive stability, collision recovery, and additional flight results).

To demonstrate controlled hovering flight, we design a four-actuator, eight-winged robot (Fig. 1e) and use a motion tracking system³ and off-board computation for sensing and control (see Supplementary Information section S4, Extended Data Fig. 10, and Extended Data Table 3 for details on the controller design, implementation, experimental validation and repeatability). Figure 4e shows composite images of a 16-s hovering flight, and the red dot indicates the setpoint (desired hovering position). Figure 4f shows the corresponding trajectory of the same flight (Supplementary Video 7), and the colour scale represents the distance from the current position to the setpoint. For this

16-s flight, the maximum deviation of altitude, lateral position, and body angles are 12 mm (0.2 body length (BL)), 36 mm (0.6 BL) and 9°, respectively (Fig. 4g–i).

To summarize, these flights demonstrate the use of soft artificial muscles as wing actuators having sufficient power density to enable lift-off and having adequate bandwidth for flight control. Compared to the state-of-the-art MAVs driven by microscale rigid actuators (<500 mg), these soft-actuator robots have advantages such as in-flight robustness to collisions and self-sensing. A feature of the DEA's fabrication scalability is that it enables efficient production of robotic modules that can be assembled in different configurations for various functions. These properties will be important for enabling swarm flight of MAVs in highly cluttered environments where collisions are difficult to avoid. However, compared to a recent piezoelectric-actuator-driven MAV³² that can demonstrate power-autonomous takeoff flights, this robot consumes 15 times more input power and requires a drive voltage 6.5 times higher. The robot's weight and

net lift are 170% and 75% that of the state-of-the-art piezoelectric-driven vehicle.

To enable power-autonomous flight in soft aerial robots, future studies need to reduce a soft actuator's operating voltage, improve its power efficiency and further increase its power density. Reducing actuation voltage is crucial because up to 75% of the input electrical power can be dissipated by compact high-voltage boost and drive circuitry (as in a recent power-autonomous MAV³²). This challenge of lowering driving voltage can be tackled by refining DEA multi-layering techniques to further reduce the elastomer layer's thickness. Towards improving transduction efficiency, future studies could incorporate new architectures of electrically actuated soft actuators such as the electrohydraulic Peano-HASEL³³ actuators, which can use flexible metallic electrodes to reduce resistive losses. To increase power density, electroactive polymers with higher dielectric strengths and lower viscoelasticity should be explored and incorporated into future soft artificial flight muscles. From a robot design perspective, scaling up the vehicle size can substantially mitigate the challenges associated with achieving power autonomy. A larger vehicle size can provide a larger net payload, which allows the robot to carry a larger and more efficient boost circuit. In addition, scaling up the wing size corresponds to a reduction of operating frequency and leads to a linear increase in the DEA's power efficiency (see Methods section 'DEA performance characterization' and Supplementary Information S5 for a detailed discussion on future directions to achieve power autonomous flights). More broadly, our work demonstrates that soft-actuated robots can be agile, robust and controllable. These characteristics are important for developing future generations of soft robots for diverse applications such as environmental exploration and manipulation.

Online content

Any methods, additional references, Nature Research reporting summaries, source data, extended data, supplementary information, acknowledgements, peer review information; details of author contributions and competing interests; and statements of data and code availability are available at <https://doi.org/10.1038/s41586-019-1737-7>.

1. Dickerson, A. K., Shankles, P. G., Madhavan, N. M. & Hu, D. L. Mosquitoes survive raindrop collisions by virtue of their low mass. *Proc. Natl Acad. Sci. USA* **109**, 9822–9827 (2012).
2. Mountcastle, A. M. & Combes, S. A. Biomechanical strategies for mitigating collision damage in insect wings: structural design versus embedded elastic materials. *J. Exp. Biol.* **217**, 1108–1115 (2014).
3. Ma, K. Y., Chirarattananon, P., Fuller, S. B. & Wood, R. J. Controlled flight of a biologically inspired, insect-scale robot. *Science* **340**, 603–607 (2013).
4. Chen, Y. et al. A biologically inspired, flapping-wing, hybrid aerial-aquatic microrobot. *Sci. Robot.* **2**, eaao5619 (2017).
5. Zou, Y., Zhang, W. & Zhang, Z. Liftoff of an electromagnetically driven insect-inspired flapping-wing robot. *IEEE Trans. Robot.* **32**, 1285–1289 (2016).
6. de Croon, G. C. H. E., De Clercq, K. M. E., Ruijsink, R., Remes, B. & De Wagter, C. Design, aerodynamics, and vision-based control of the DelFly. *Int. J. Micro Air Veh.* **1**, 71–97 (2009).
7. Carpi, F., Bauer, S. & Rossi, D. D. Stretching dielectric elastomer performance. *Science* **330**, 1759–1761 (2010).
8. Rosset, S. & Shea, H. R. Flexible and stretchable electrodes for dielectric elastomer actuators. *Appl. Phys. A* **110**, 281–307 (2013).

9. Zhao, H. et al. Compact dielectric elastomer linear actuators. *Adv. Funct. Mater.* **28**, 1804328 (2018).
10. Acome, E. et al. Hydraulically amplified self-healing electrostatic actuators with muscle-like performance. *Science* **359**, 61–65 (2018).
11. Pelrine, R. et al. Dielectric elastomer artificial muscle actuators: toward biomimetic motion. In *Smart Structures and Materials 2002: Electroactive Polymer Actuators And Devices (EAPAD)* Vol. **4695**, 126–137 (International Society for Optics and Photonics, 2002); <https://www.spiedigitallibrary.org/conference-proceedings-of-spie/4695/0000/Dielectric-elastomer-artificial-muscle-actuators-toward-biomimetic-motion/10.1117/12.475157.full>.
12. Zhao, J., Niu, J., McCoul, D., Leng, J. & Pei, Q. A rotary joint for a flapping wing actuated by dielectric elastomers: design and experiment. *Mecanica* **50**, 2815–2824 (2015).
13. Lau, G.-K., Lim, H.-T., Teo, J.-Y. & Chin, Y.-W. Lightweight mechanical amplifiers for rolled dielectric elastomer actuators and their integration with bio-inspired wing flappers. *Smart Mater. Struct.* **23**, 025021 (2014).
14. Shepherd, R. F. et al. Multigait soft robot. *Proc. Natl Acad. Sci. USA* **108**, 20400–20403 (2011).
15. Rus, D. & Tolley, M. T. Design, fabrication and control of soft robots. *Nature* **521**, 467–475 (2015).
16. Majidi, C. Soft robotics: a perspective—current trends and prospects for the future. *Soft Robot.* **1**, 5–11 (2014).
17. Choe, K. et al. Performance characteristics of electro-chemically driven polyacrylonitrile fiber bundle actuators. *J. Intell. Mater. Syst. Struct.* **17**, 563–576 (2006).
18. Suzumori, K., Iikura, S. & Tanaka, H. Applying a flexible microactuator to robotic mechanisms. *IEEE Contr. Syst. Mag.* **12**, 21–27 (1992).
19. Onal, C. D., Chen, X., Whitesides, G. M. & Rus, D. Soft mobile robots with on-board chemical pressure generation. In *Robotics Research* 525–540 (Springer, 2017).
20. Katschmann, R. K., Marchese, A. D. & Rus, D. Hydraulic autonomous soft robotic fish for 3D swimming. In *Experimental Robotics* 405–420 (Springer, 2016).
21. Loomis, J., Xu, P. & Panchapakesan, B. Stimuli-responsive transformation in carbon nanotube/expanding microsphere-polymer composites. *Nanotechnology* **24**, 185703 (2013).
22. Cheng, N. G., Gopinath, A., Wang, L., Iagnemma, K. & Hosoi, A. E. Thermally tunable, self-healing composites for soft robotic applications. *Macromol. Mater. Eng.* **299**, 1279–1284 (2014).
23. Sadeghipour, K., Salomon, R. & Neogi, S. Development of a novel electrochemically active membrane and 'smart' material based vibration sensor/damper. *Smart Mater. Struct.* **1**, 172 (1992).
24. Pei, Q., Rosenthal, M., Stanford, S., Prahlad, H. & Pelrine, R. Multiple-degrees-of-freedom electroelastomer roll actuators. *Smart Mater. Struct.* **13**, N86 (2004).
25. Shian, S., Bertoldi, K. & Clarke, D. R. Use of aligned fibers to enhance the performance of dielectric elastomer inchworm robots. In *Electroactive Polymer Actuators and Devices (EAPAD) 94301P* (International Society for Optics and Photonics, 2015); <https://www.spiedigitallibrary.org/conference-proceedings-of-spie/9430/94301P/Use-of-aligned-fibers-to-enhance-the-performance-of-dielectric/10.1117/12.2084140.full>.
26. Li, T. et al. Fast-moving soft electronic fish. *Sci. Adv.* **3**, e1602045 (2017).
27. Berliner, F. et al. A modular dielectric elastomer actuator to drive miniature autonomous underwater vehicles. In *IEEE Int. Conf. on Robotics and Automation (ICRA)*. 3429–3435 (IEEE, 2018).
28. Dickinson, M. H. Muscle efficiency and elastic storage in the flight motor of *Drosophila*. *Science* **268**, 87–90 (1995).
29. Chen, Y., Gravish, N., Desbiens, A. L., Malka, R. & Wood, R. J. Experimental and computational studies of the aerodynamic performance of a flapping and passively rotating insect wing. *J. Fluid Mech.* **791**, 1–33 (2016).
30. Tu, Z., Fei, F., Zhang, J. & Deng, X. Acting is seeing: navigating tight space using flapping wings. Preprint at <https://arxiv.org/abs/1902.08688> (2019).
31. Jayaram, K., Jafferis, N. T., Doshi, N., Goldberg, B. & Wood, R. J. Concomitant sensing and actuation for piezoelectric microrobots. *Smart Mater. Struct.* **27**, 065028 (2018).
32. Jafferis, N. T., Helbling, E. F., Karpelson, M. & Wood, R. J. Untethered flight of an insect-sized flapping-wing microscale aerial vehicle. *Nature* **570**, 491–495 (2019).
33. Kellaris, N., Venkata, V. G., Smith, G. M., Mitchell, S. K. & Keplinger, C. Peano-HASEL actuators: muscle-mimetic, electrohydraulic transducers that linearly contract on activation. *Sci. Robot.* **3**, eaar3276 (2018).

Publisher's note Springer Nature remains neutral with regard to jurisdictional claims in published maps and institutional affiliations.

© The Author(s), under exclusive licence to Springer Nature Limited 2019

Article

Methods

Conceptual design of a DEA-powered aerial robot

The DEA-powered robot consists of five major components: an actuator, an airframe, transmission, two wing hinges and two wings. The two ends of the DEA are connected to the robot transmission, and the DEA's linear actuation is converted to the flapping motion of both wings. The structural design of this robot is similar to that of a microrobot powered by piezoelectric actuators that was presented in a previous study³⁴. However, we needed to redesign each component to accommodate the soft actuator. In the following, we describe the design process to determine key robot parameters and present the requirements on DEA performance.

To achieve takeoff, the DEA must satisfy requirements for blocked force, resonant frequency, free displacement and power density. Specifically, the actuator needs to meet two conditions. First, the robot wings need to flap at sufficient frequency with adequate amplitude to generate a lift force that balances the robot weight. This condition places requirements on the DEA's operating frequency and displacement. Rearranging the equation that imposes the lift force and robot weight balance leads to the relationship:

$$f\delta = \frac{1}{2\pi\hat{r}_2 R^2 T} \sqrt{\frac{AR \times W f_m}{C_L \rho}} \quad (1)$$

where f is the robot's operating frequency, δ is half of the DEA's free displacement at the frequency f , \hat{r}_2 is the wing's second area moment, R is the wing span, T is the transmission ratio, AR is the wing's aspect ratio, W is the robot's weight, C_L is the mean lift coefficient, ρ is the air density, and f_m is a mass scaling ratio such that the extra lift force can be used for flight control. In addition to satisfying this kinematic condition, the DEA needs to overcome the aerodynamic drag force during flight, and this imposes a requirement on the DEA's blocked force:

$$F_B = 2\sqrt{2} Tr_{cp} W f_m \frac{\bar{C}_D}{\bar{C}_L} \quad (2)$$

where F_B is the DEA's blocked force, r_{cp} is the wing's spanwise centre of pressure, and \bar{C}_D is the time-averaged drag coefficient. The derivation of equations (1) and (2) follows closely from equations (1) to (14) in a previous work³⁴. In equations (1) and (2), we assume that the DEA's blocked force is independent of its actuation frequency. This assumption is validated in the next section on DEA characterization. Multiplying equations (1) and (2) gives a requirement for the DEA's output mechanical power.

The design of a DEA-powered aerial robot also needs to satisfy an additional condition because the DEA's actuation is nonlinear with respect to input voltage. With a sinusoidal input, the DEA's actuation contains higher-order harmonics that can adversely affect flapping-wing kinematics. As discussed in the main text, we attenuate higher-order harmonics by setting the robot operating frequency close to the natural frequency of the DEA-transmission-wing system. A previous study³⁴ shows that the actuator-transmission-wing system can be described by a lumped-parameter model. The system resonant frequency is given by:

$$f = 2\pi \sqrt{\frac{k_m + k_t T^2}{m_a + 2T^2 I_{zz}}} \quad (3)$$

where k_m is the DEA's intrinsic stiffness, m_a is the DEA's mass, k_t is the transmission's torsional stiffness, and I_{zz} is the wing's moment of inertia relative to the stroke rotational axis. For our robot, the transmission stiffness is much lower than the DEA's effective stiffness. To obtain a higher operating frequency, this condition requires a smaller wing moment of inertia. The wing moment of inertia can be decreased by

reducing wing size. Using equations (1) to (3), we select values for the transmission ratio and the wing size while satisfying constraints imposed by our fabrication methods (that is, minimum feature size, wing inertia and so on). The values of these design parameters are reported in Extended Data Table 1. Using these parameters, we obtain the following requirements for a 100-mg DEA: $F_B = 0.2\text{ N}$, $f = 290\text{ Hz}$, and $\delta = 0.3\text{ mm}$. Multiplying these parameters shows that the DEA needs to have a minimum output power density of 200 W kg^{-1} . This requirement is similar to that for the MAVs powered by piezoelectric actuators³ and to the power density values estimated for flying insects.

Fabrication of robot components

The robot airframe, transmission, wings and wing hinges are made using an existing multi-scale, multi-material fabrication method³⁵. The airframe consists of eight pieces of 160-μm carbon fibre laminates assembled manually and reinforced with glue (Loctite 495) (Extended Data Fig. 1a). The robot transmission is a planar four-bar mechanism. The transmission ratio is approximated as $T = l_3^{-1}$, where the link length l_3 is marked in Extended Data Fig. 1b. The robot transmission is attached to the DEA via a fibreglass connector, which insulates the robot structure from the DEA's driving signals. Further, the transmission connects the airframe and the wing hinge. A wing is attached onto the robot's wing hinge. The wing hinge and wing are designed according to an existing method³⁶, and their geometries are illustrated in Extended Data Fig. 1c and d.

The DEA takes the form of a cylindrical shell, whose height and radius determine the actuation frequency, blocked force and free displacement. The DEA is made of a multi-layering process⁹, and it is rolled from a rectangular elastomer sheet that has embedded electrodes. Since the DEA drives two wings simultaneously, its free displacement needs to be larger than 600 μm (twice the value of the design parameter δ). Based on the values of DEA free displacement, peak loading, and elastomer stiffness, we set the actuator length to 8 mm. To obtain a blocked force over 0.2 N, the elastomer sheet (before roll-up) width is set to 5 cm. This elastomer sheet is approximately 220 μm thick, and it is manually rolled into a cylindrical shell whose inner and outer diameters are 1.5 mm and 4.5 mm, respectively.

The elastomer is a 5:4 mixture of Ecoflex 0030 (Smooth-On) and Sylgard 184 (Dow Corning). The ratio of crosslinker in Sylgard 184 is 1:40. We put a thin layer of carbon nanotube (CNT) (from Nano-C) on the elastomer and use it as the DEA's compliant electrode. For coating the electrode, we use 150 μl of CNT solution over a 90-mm-diameter polytetrafluoroethylene (PTFE) filter (Satorius 7022P). The procedures for elastomer preparation, spin coating and electrode patterning are adopted from a previous study⁹.

We made several modifications to the fabrication process to increase DEA power density and endurance. First, DEA power density can be increased by having an even number of CNT layers. Extended Data Fig. 1e shows the rolling process of a multi-layered DEA. We use grey-coloured regions to denote the elastomer layers. The positive and negative electrodes are represented by red and black lines, respectively. We represent the bottom elastomer layer with a darker grey colour. When the elastomer sheet is rolled into a cylindrical shell, the DEA's bottom layer is put into contact with its top layer. This is illustrated by the inset shown in Extended Data Fig. 1f. The region highlighted by blue lines further shows that a new layer is formed by the DEA's top and bottom elastomer layers and electrodes. If the top and bottom electrodes are oppositely charged (as illustrated in Extended Data Fig. 1f), then this effective layer develops an electric field and contributes to actuation. We must have an even number of electrode layers to ensure that the bottom and top electrodes are oppositely charged.

In this work, our DEA design has six CNT and seven elastomer layers. Further, if the top and bottom elastomer layers have the same thickness as all other layers, then the electric field in this new layer is only half that of other layers because the effective layer thickness is $t_{top} +$

t_{bottom} (Extended Data Fig. 1g). Hence, reducing the top- and bottom-layer thickness increases the electric field in the additional layer, and this results in an increase in DEA output power. We use a faster spin-coating speed (2,700 revolutions per minute) for the top and bottom layer and a slower speed (1,700 revolutions per minute) for the middle layers. Through reducing the top and bottom elastomer layer thickness by approximately 35% (Extended Data Fig. 1h), we obtain an 11% mass reduction and a 9% increase in output power relative to a DEA with constant elastomer layer thickness. After making the elastomer layers and transferring the electrodes, we cut out the DEA from the elastomer substrate and roll it into a cylindrical shell. In the previous study⁹, the DEA is cut out manually with a razor blade. Our application requires higher accuracy, so we program a digital cutter (Silhouette Cameo) to cut out the DEA. The DEA's length is set to 8.6 mm including the exposed CNT tabs for electrical connection. With this modification, variation in the DEA length is reduced to within 150 μm . Having a precise DEA length is crucial for attaching the DEA to the robot transmission during assembly.

In addition, the DEA's bandwidth depends on several factors such as elastomer mechanical viscoelasticity ($\tan\delta$), DEA geometry, and electrode conductivity. Here, we improve the fabrication process relative to a previous study⁹ to ensure good conductivity during DEA actuation (Extended Data Fig. 1i). After the DEA is rolled into a shell, carbon conductive adhesive (Electron Microscopy Sciences) is applied to the exposed electrodes and carbon fibre endcaps are glued to each end. For driving our flapping wing robot, the DEA needs to overcome aerodynamic drag during both elongation and retraction phases. During DEA retraction, aerodynamic drag opposes the DEA motion and applies a tensile stress on the DEA connections. At peak loading, this tensile stress weakens the bonding between the elastomer and the endcap, and it can create local tears and further lead to delamination. This delamination reduces electrical conductivity, which increases the DEA's time constant and reduces its bandwidth. We overcome this problem by modifying the fabrication process to increase the endcap adhesion strength. During fabrication, Loctite 416 is applied to the outer perimeter of the elastomer shell and the endcaps. The DEA is compressed with a mass of 18 g and then baked at 72 °C for 4 h. The glue cures in this process and holds the electrical connections in compression. The preload is removed after the glue cures, and other regions of the DEA return to a neutral state. A photograph of the DEA is shown in Extended Data Fig. 1j. With this procedure, we obtain an approximately four-fold increase in DEA conductivity compared to those made using previous methods⁹.

DEA performance characterization

Here we describe the experimental characterization of the DEA's blocked force, free displacement, bandwidth, power consumption and efficiency. To measure the DEA's blocked force, we place the DEA under a force sensor (Nano 17 Titanium). The sensor is mounted on a two-axis stage and is lowered until it touches the DEA's top cap (Extended Data Fig. 2a). To ensure the DEA remains securely affixed under the sensor during its retraction phase, we continue lowering the sensor to induce a preload of approximately 0.05 N. The sensor resolution and the resonant frequency are 1.5 mN and 3,000 Hz, respectively. We sample the sensor reading at 10 kHz and apply a 1,500-Hz non-causal low-pass filter to post-process the data. To measure the DEA's free displacement, we place a DEA under a laser vibrometer (Polytec PSV-500). The vibrometer measures the instantaneous velocity of the DEA's oscillatory motion (Extended Data Fig. 2b) approximately 40 times per period. For time sequence measurements, the vibrometer averages over five cycles to reduce measurement noise. The measured velocity is integrated numerically to calculate the DEA displacement. In addition, the vibrometer can measure the DEA's frequency response by driving the DEA with white noise and computing the FFT of the displacement. This measurement gives a linear approximation of the device frequency response. It quantifies the DEA's resonant modes

and phase shift (Fig. 2c, d). This information is useful for robot design because the DEA's motion is approximated as linear around system resonance at flight conditions.

Sample experimental measurements of blocked force and free displacement are shown in Extended Data Fig. 2c and d, respectively. In these experiments, the DEA is driven at 350 Hz and 1,300 V. The amplitude of the DEA's blocked force is calculated as the maximum value of the measured force and it does not include the preload force (the range is labelled by the red arrows in Extended Data Fig. 2c). In our experiments, we vary the preload in the range of 0.025 N to 0.1 N and find that the magnitude of preload has a negligible effect on the blocked force measurement. The amplitude of the DEA's free displacement is calculated as the difference between the maximum and the minimum value (as indicated by the red arrows in Extended Data Fig. 2d). We report the peak-to-peak displacement value because the DEA does mechanical work during both elongation and retraction. To characterize DEA performance for different operating conditions (Fig. 2a, b), we vary input voltage amplitudes and driving frequencies from 800 V to 1,300 V, and from 1 Hz to 600 Hz. Based on the force and displacement measurements, the actuator energy and power density are calculated as:

$$e = \frac{1}{2m_a} F_B \delta \quad (4)$$

$$p = \frac{1}{2m_a} F_B \delta f \quad (5)$$

Equations (4) and 5 assume the elastomer's stress-strain relationship is approximately linear. Through conducting tensile tests using an Instron materials testing machine, we find that the elastomer exhibits a linear response for a strain less than 20%. The elastomer Young's modulus is measured to be 140 kPa. The maximum measured energy density (Extended Data Fig. 2e) and power density (Extended Data Fig. 2f) are 1.13 J kg⁻¹ and 563 W kg⁻¹, respectively (at 500 Hz and 1,300 V). These values satisfy the criteria for robot takeoff (Supplementary Information section S1). The DEA's driving voltage can be further increased to 1,500 V in controlled hovering flight demonstrations, so the DEA's peak power density is estimated to be 15% higher than the reported value. The DEA experiences dielectric breakdown for a driving voltage higher than 1,500 V.

In our flight experiments, the robot is driven by an external power source through a thin tether. Here we quantify the DEA's resistance, capacitance, power consumption and efficiency. These parameters are important for achieving power autonomous flights in future studies. To quantify the DEA's power consumption, we measure the DEA's input voltage (V) and corresponding current (I) at flight conditions. The average electrical power input is:

$$\bar{P}_{\text{in}} = \frac{1}{T} \int_0^T V(t) I(t) dt \quad (6)$$

A sample measurement of instantaneous power is shown in Extended Data Fig. 2g, in which the average power consumption is 450 mW. We further measure the DEA's resistance and capacitance by sending a step input and measuring the corresponding current response. The system is modelled as a RC circuit, and parameters such as series resistance, capacitance and time constant can be obtained by fitting a first-order system to the current response. The DEA's resistance, capacitance, and time constant are 170 k Ω , 1.04 nF and 178 μs , respectively. Having calculated the DEA's resistance, we further compute the average power dissipated due to electrical resistance:

$$\bar{P}_{\text{ele}} = \frac{R}{T} \int_0^T I^2(t) dt \quad (7)$$

Article

The DEA electrode dissipates 330 mW of power at flight conditions. The mechanical power output at this operating condition is calculated as $P = \frac{1}{2}F_B\delta f$, where the values of F_B , δ and f are 0.19 N, 0.89 mm and 300 Hz, respectively. The estimated power output is 25 mW, which implies that the DEA efficiency is 5.6%. Over 73% of the power is dissipated by the electrode resistance, and the rest of the power dissipation is contributed by the elastomer's viscoelastic damping.

This power dissipation leads to substantial heating of the DEA. The system can be described by a first-order conduction model:

$$\frac{dT}{dt} = -K(T - T_a) + \frac{Q}{C} \quad (8)$$

where T is the DEA temperature, T_a is the ambient temperature, K is the dissipation rate, Q is the heat inflow, and C is the DEA's heat capacity. This first-order differential equation has a closed form solution. The solutions for the rising and the cooling phases are:

$$T_{\text{rise}} = T_a + \frac{Q}{cK_1}(1 - e^{-K_1 t}) \quad (9)$$

$$T_{\text{cool}} = T_a + (T_i - T_a)e^{-K_2 t} \quad (10)$$

where T_i is the initial temperature at the onset of cool down. The dissipation coefficients (K_1 and K_2) in the heating and the cooling phases are different because the flapping motion during the heating phase induces an airflow that facilitates convective cooling. The values of these modelling parameters are reported in Extended Data Table 1.

We use a FLIR T440 thermal camera to measure the DEA temperature when the robot operates under takeoff conditions (Extended Data Fig. 2h). The DEA temperature increases from 28 °C to 70 °C in 90 s. An analytical fit is superimposed on the same graph (Extended Data Fig. 2h). Snapshots of a thermal video are shown in Extended Data Fig. 2i. The maximum DEA temperature reaches 70.0 °C before cool down. This experiment shows most of the input electrical power is dissipated in the form of heat. Generating excessive amount of heat can lead to thermal failure and reduce actuator lifetime. Through our experiments, we find that our DEA can operate for over 600,000 cycles under takeoff conditions, equivalent to 33 min of flight time.

In this study, our DEA has a low transduction efficiency of 5.6%. This low transduction efficiency would not be conducive to power-autonomous flights. In addition, it requires a 1,300V driving signal to achieve takeoff, which creates challenges for developing high-efficiency boost circuitry. Although this study does not aim to achieve power-autonomous flight, it is important to identify major challenges and potential solutions. Future studies should focus on increasing the DEA electrode's conductivity, reducing elastomer layer thickness to reduce the driving voltage, and redesigning the DEA geometry and robot wings to reduce the flapping frequency. First, increasing electrode conductivity will lead to a reduction of resistive power loss. This can be done by exploring new electrode materials such as a hybrid network of carbon nanotubes, graphene and silver nanowires³⁷ or intrinsically stretchable electrodes such as conductive hydrogels³⁸ or liquid metal. Second, reducing elastomer thickness will reduce the operating voltage. We can achieve this by increasing the spin-coating speed or exploring

alternative method such as using an automatic thin film applicator. Further, the spin coating and the electrode transfer process can be done in a clean room environment to reduce the number of particulates in the elastomer and on the electrodes. Third, new electroactive materials such as bottlebrush elastomers³⁹ can be explored to further increase the actuator's energy density. In addition, our experiments show that DEA power consumption is linearly proportional to its operating frequency. To reduce power expenditure, future studies can redesign the DEA geometry and robot transmission to reduce system resonant frequency. Alternatively, nonlinear controllers can be developed so that the DEA motion does not need to be linearized around its resonance. Beyond improving the DEAs, we can apply a new class of electrostatic actuators named Peano-HASEL^{33,40} that have shown promise for achieving very high energy density and moderate bandwidth. For that class of actuators, it would be important to work on device miniaturization to reduce the driving voltage.

Data availability

All data generated or analysed for this paper are included in the published article, its Methods, and its Supplementary Information. Original videos, computer code and sensor data are available from the corresponding author on reasonable request.

34. Whitney, J. P. & Wood, R. J. Conceptual design of flapping-wing micro air vehicles. *Bioinspir. Biomim.* **7**, 036001 (2012).
35. Whitney, J. P., Sreetharan, P. S., Ma, K. Y. & Wood, R. J. Pop-up book MEMS. *J. Micromech. Microeng.* **21**, 115021 (2011).
36. Chen, Y., Ma, K. & Wood, R. J. Influence of wing morphological and inertial parameters on flapping flight performance. In *IEEE/RSJ Int. Conf. on Intelligent Robots and Systems* 2329–2336 (IEEE, 2016).
37. Liang, J. et al. Intrinsically stretchable and transparent thin-film transistors based on printable silver nanowires, carbon nanotubes and an elastomeric dielectric. *Nat. Commun.* **6**, 7647 (2015).
38. Keplinger, C. et al. Stretchable, transparent, ionic conductors. *Science* **341**, 984–987 (2013).
39. Vatankhah-Varnoosfaderani, M. et al. Bottlebrush elastomers: a new platform for freestanding electroactuation. *Adv. Mater.* **29**, 1604209 (2017).
40. Kellaris, N., Venkata, V. G., Rothemund, P. & Keplinger, C. An analytical model for the design of Peano-HASEL actuators with drastically improved performance. *Extreme Mech. Lett.* **29**, 100449 (2019).

Acknowledgements We thank Y. Zhu for comments and discussion. This work is supported by the National Science Foundation (award number CMMI-1830291) and the Wyss Institute for Biologically Inspired Engineering. In addition, the prototypes were enabled by equipment supported by the Army Research Office DURIP programme (award number W911NF-13-1-0311). Any opinions, findings and conclusions or recommendations expressed in this material are those of the authors and do not necessarily reflect the views of the National Science Foundation.

Author contributions Y.C., H.Z., and R.J.W. proposed and designed the research. Y.C., H.Z. and J.M. built the robot. Y.C., H.Z., J.M., P.C. and E.F.H. conducted the experimental work. Y.C., H.Z., P.C., N.-s.P.H., D.R.C. and R.J.W. contributed to modelling and data analysis. Y.C. wrote the paper. All authors provided feedback.

Competing interests The authors declare no competing interests.

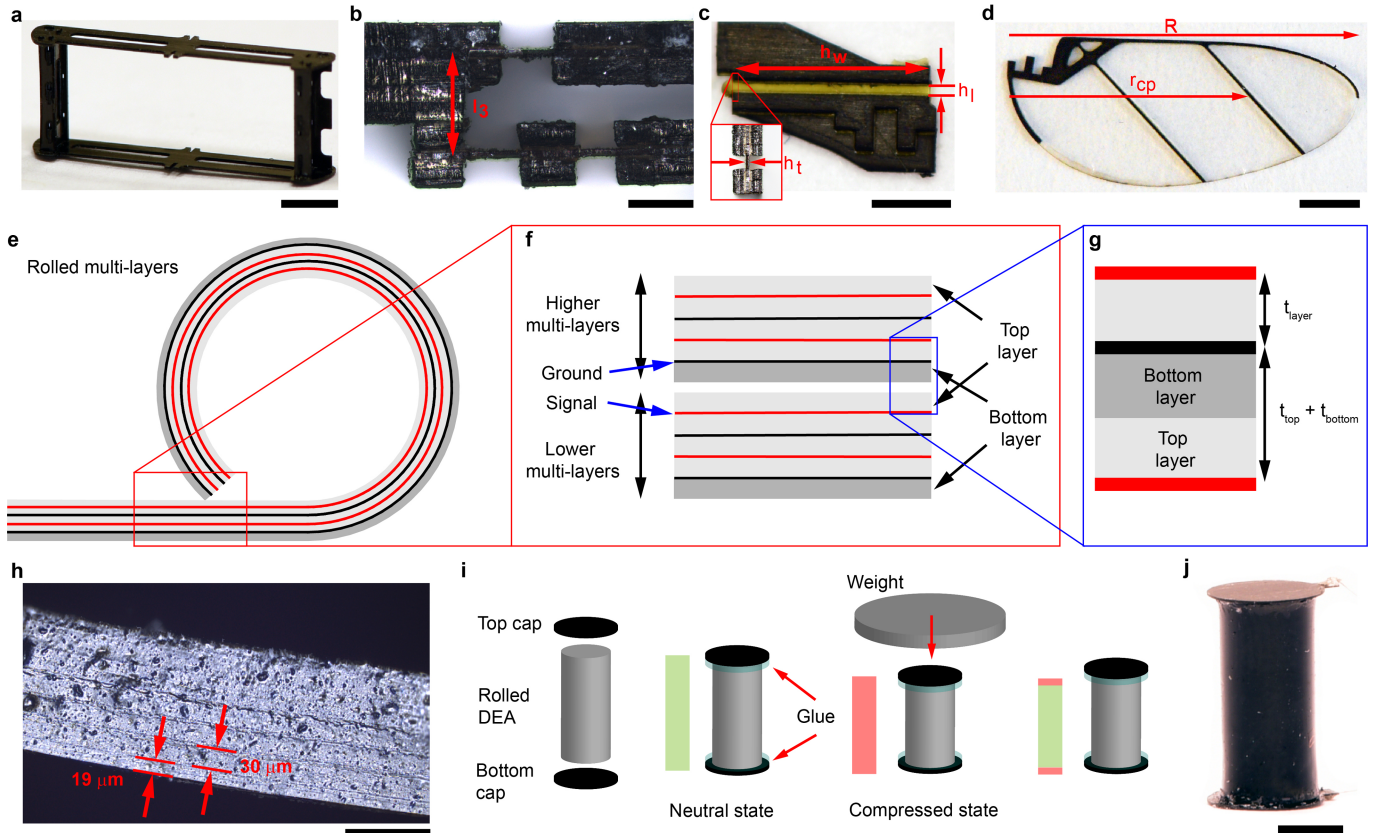
Additional information

Supplementary information is available for this paper at <https://doi.org/10.1038/s41586-019-1737-7>.

Correspondence and requests for materials should be addressed to Y.C. or R.J.W.

Peer review information *Nature* thanks Dario Floreano, Christoph Keplinger and the other, anonymous, reviewer(s) for their contribution to the peer review of this work.

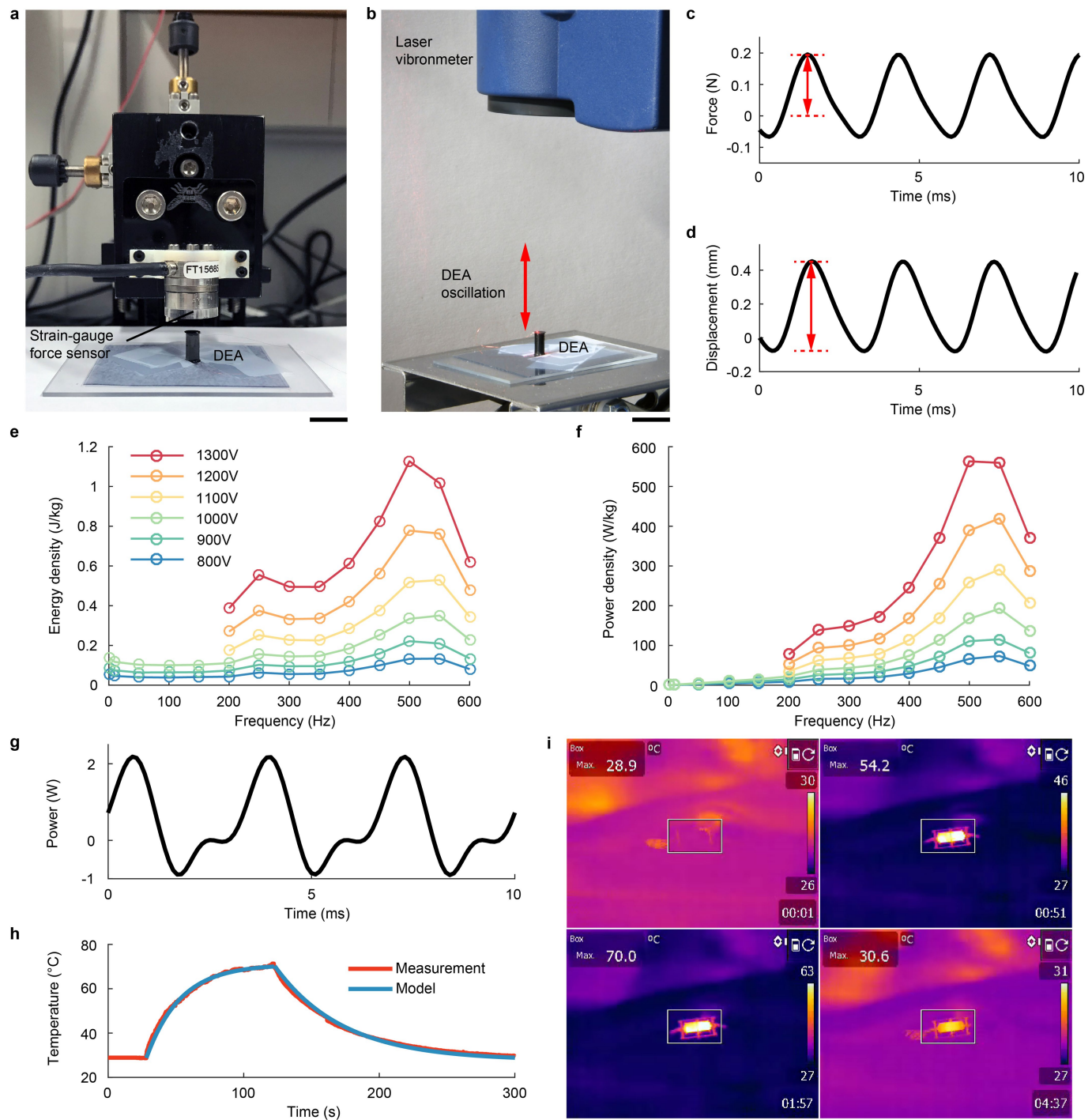
Reprints and permissions information is available at <http://www.nature.com/reprints>.



Extended Data Fig. 1 | Design and fabrication of robot components. **a**, A 40-mg airframe made of eight pieces of carbon fibre composites. Scale bar represents 2 mm. **b**, Top view of the planar four-bar transmission. The red arrow marks l_3 , which is the inverse of the transmission ratio T . Scale bar represents 200 μm . **c**, Front view of the wing hinge. The hinge width (h_w), length (h_l), and thickness (h_t) determine its torsional stiffness. Scale bar represents 1 mm. **d**, Front view of a robot wing whose wing span (R) and centre of pressure (r_{cp}) are 10 mm and 7 mm, respectively. Scale bar represents 2 mm. **e**, An illustration of rolling an elastomer-electrode multilayer into a DEA. **f**, A zoomed-in illustration of the inset shown in **e**. **g**, A zoomed-in illustration of the inset shown in **e**.

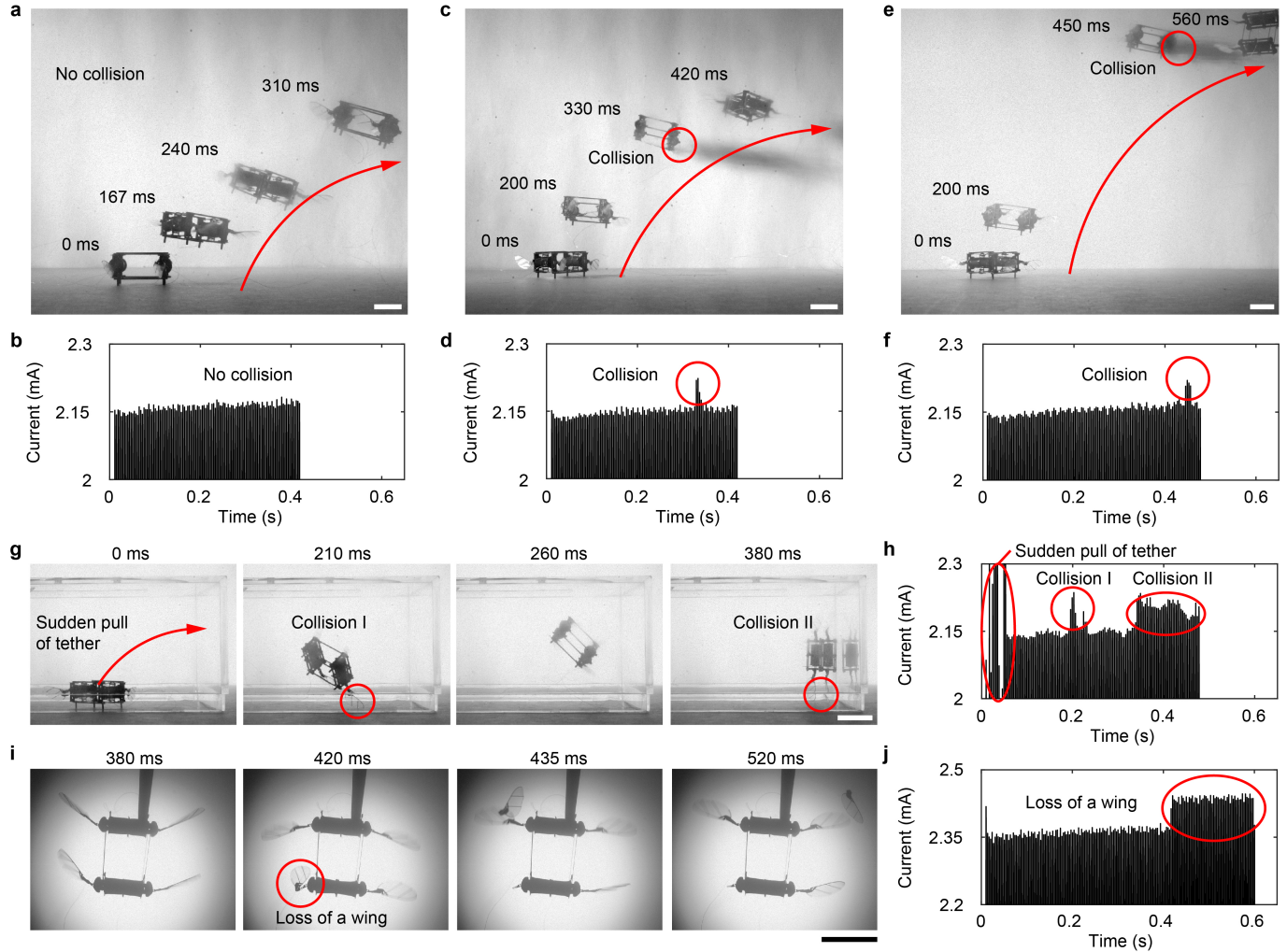
shown in **f**. The bottom layer of the top multi-layer and the top layer of the bottom multi-layer forms a region that can be actuated. **h**, Confocal microscopy image of the DEA's cross section. The elastomer sheet is 220 μm thick and it has seven elastomer layers. The thickness of the top and the bottom layers are approximately 65% of the middle layers. Scale bar represents 100 μm . **i**, Fabrication of the DEA. After the elastomer sheet is rolled into a cylindrical shell, the top and bottom cap are glued onto the DEA. A weight is placed on top of the DEA as the glue cures. After the glue cures, the DEA connections remain in compression (red) while the rest of the DEA returns to its neutral state (green). **j**, Front view of a DEA. Scale bar represents 3 mm.

Article



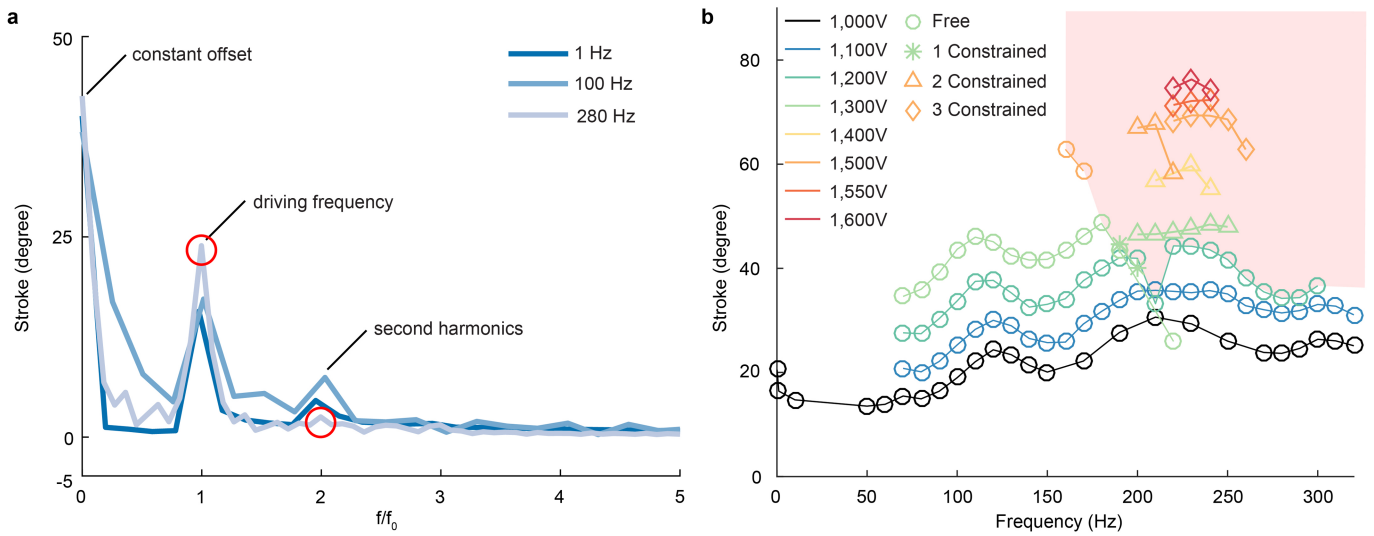
Extended Data Fig. 2 | Characterization of blocked force, free displacement and power dissipation. **a**, Experimental setup for measuring the DEA's blocked force. **b**, Experimental setup for measuring the DEA's free displacement. **c, d**, Sample blocked force (**c**) and free displacement (**d**) measurements when the DEA is driven at 350 Hz and 1,300 V. The red arrows in **c** and **d** indicate the ranges of blocked force and free displacement that correspond to Fig. 2a and b. **e, f**, The DEA's energy (**e**) and power (**f**) density as functions of driving

frequency and voltage. This DEA's blocked force and free displacement measurements are shown in Fig. 2a, b, g. The DEA's instantaneous power consumption when driven at 1,400 V and 300 Hz. **h**, Measurement and modelling of the DEA's temperature profile during its operation at 1,400 V and 300 Hz. **i**, Thermal images showing the temperature of the DEA during operation. **h** and **i** show the same experiment. Scale bars in **a**, **b** and **i** represent 1 cm.



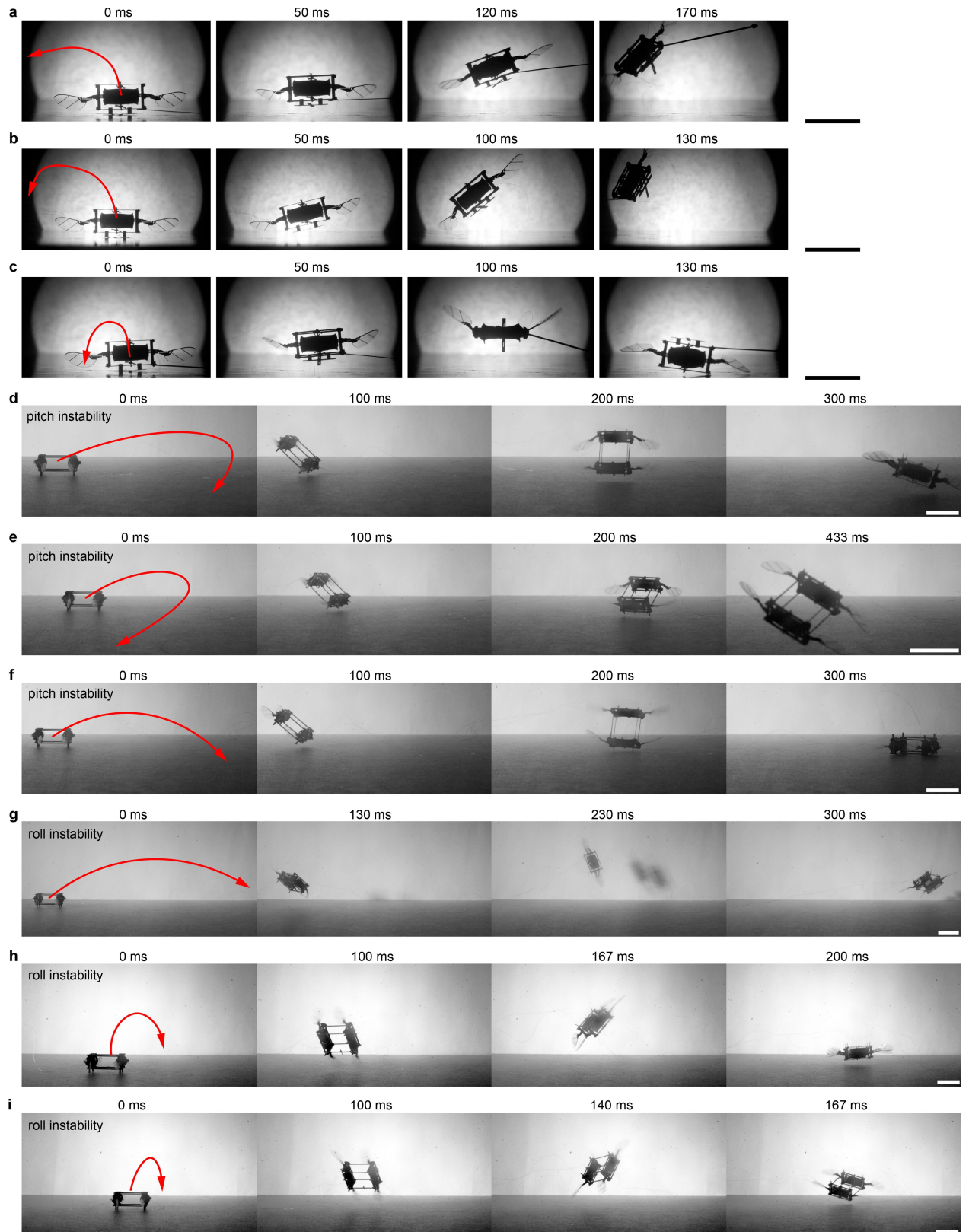
Extended Data Fig. 3 | Robot in-flight collision and damage sensing. **a, b**, A composite image (**a**) and the measured DEA current (**b**) of a short takeoff flight without any collisions. **c–f**, Two takeoff flights in which the robot hits a wall during its ascent. The red circles in **c** and **e** mark the collision events and they correspond to the current spikes in **d** and **f**, respectively. **g, h**, A robot takeoff

flight in a transparent box. The robot makes multiple collisions and the red circles in **g** and **h** relate these collisions to DEA current changes. **i, j**, An image sequence (**i**) and the measured current (**j**) of a flapping-wing characterization test. One robot wing falls off during the experiment and this event is detected by measuring the DEA current. Scale bars in **a, c, e, g** and **i** represent 1 cm.



Extended Data Fig. 4 | DEA actuation nonlinearity. **a**, FFT of the tracked wing stroke kinematics when a wing is driven at 1 Hz, 100 Hz and 280 Hz. The stroke kinematics data are taken from that shown in Fig. 3b. There is a substantial second-order harmonic for the cases of 1 Hz and 100 Hz. When the wing is driven near the system resonant frequency (280 Hz), the red circles indicate

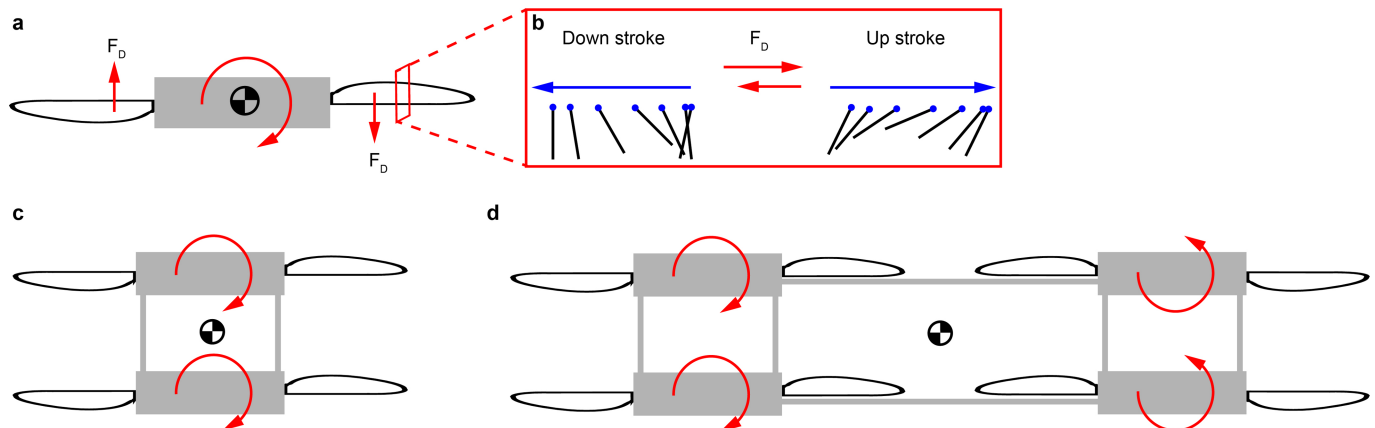
that the fundamental harmonic grows and the second harmonic is attenuated. **b**, Right wing stroke amplitude as a function of driving voltage and frequency. The red region represents stroke amplitudes and frequencies that cannot be achieved without constraining the DEA. The data correspond to the same experiment shown in Fig. 3f.



Extended Data Fig. 5 | Repeated unstable takeoff flights. **a-c**, Three takeoff flights of a robot with one DEA. In these flights, the robot flips upside down within 200 ms after lift-off owing to aerodynamic torque imbalances from the two wings. **d-i**, Unstable (pitch and roll) takeoff flights of a robot with two

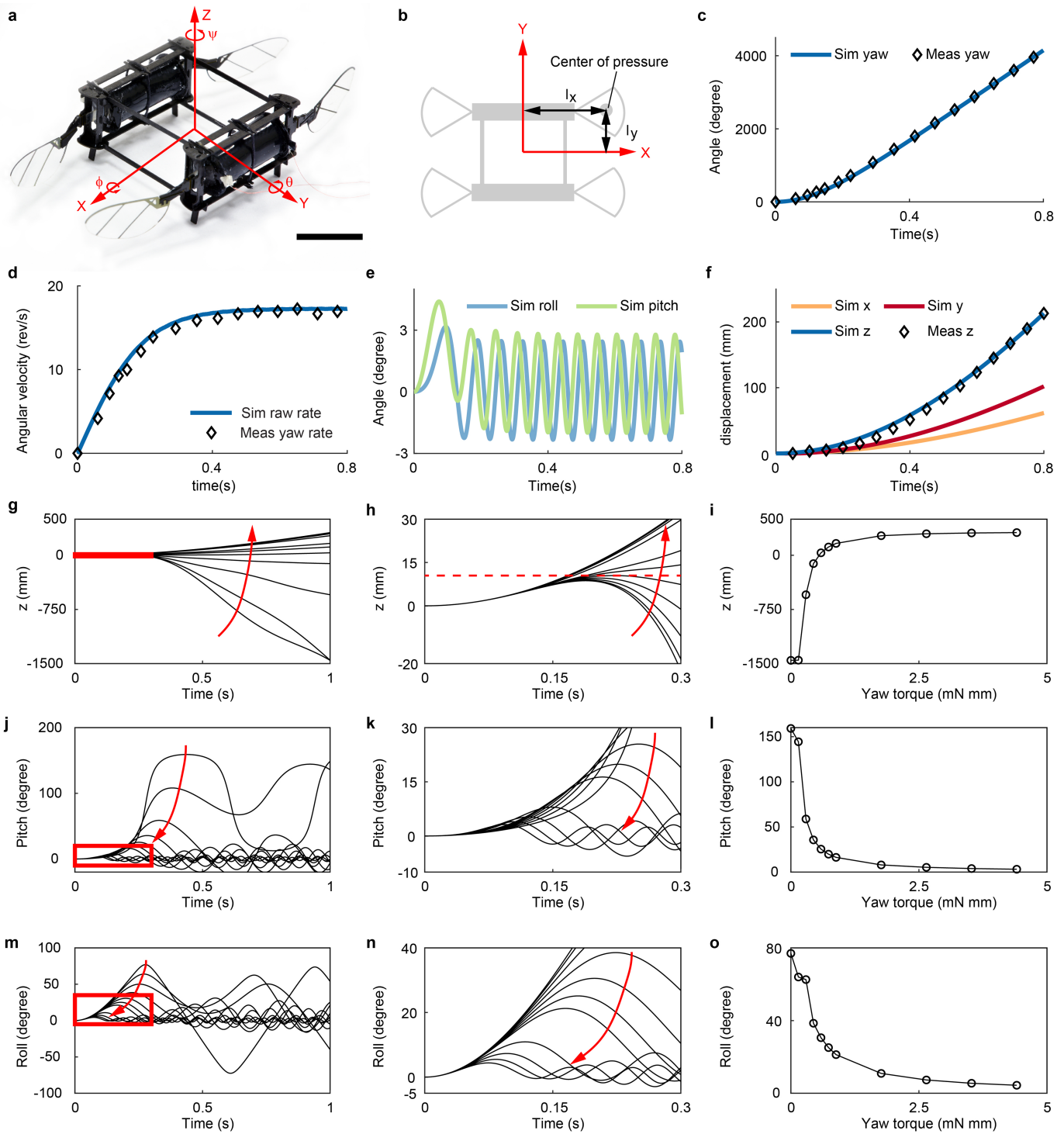
DEAs. In **d-f**, the robot pitches forward and eventually flips over owing to asymmetric lift forces from the front and the back robot modules. In **g-i**, the robot rolls sideways and flips over owing to lift force imbalances between its left and right wings. Scale bars in **a-i** represent 1 cm.

Article



Extended Data Fig. 6 | Illustration of robot yaw torque generation through biasing the mean wing pitch angle. **a**, Illustration of wing pitch bias in a one-DEA module. The red arrows indicate the directions of the mean drag force caused by biasing the wing pitch. The net drag forces from the two wings induce a robot yaw torque. **b**, The inset shows the motion of a wing chord on a two-dimensional plane. The wing pitch bias causes different wing pitching

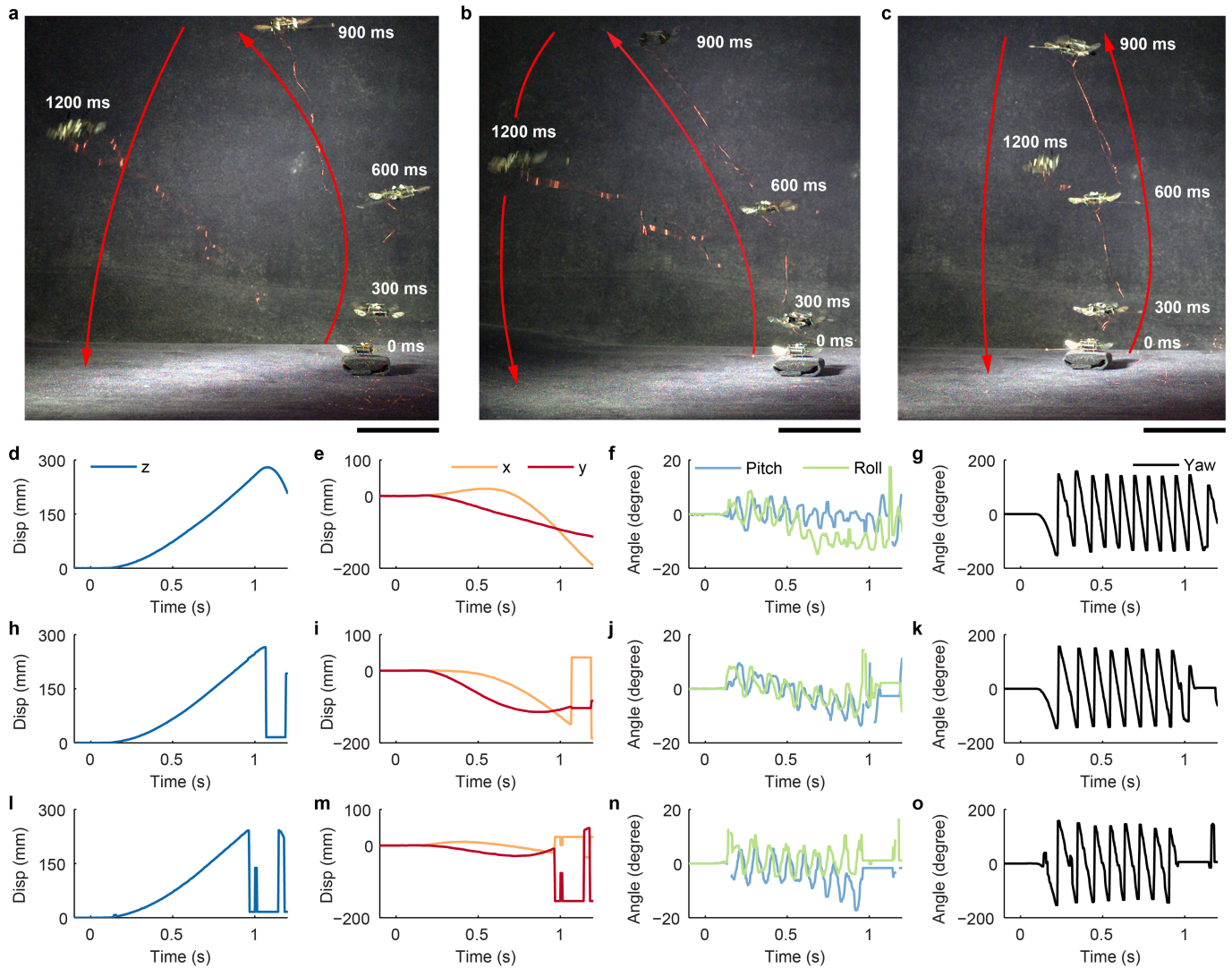
motion in the up stroke and down stroke phases of the wing motion, which leads to different drag forces. **c**, Two one-DEA modules having the same yaw torque bias direction are assembled into a two-DEA robot. **d**, Two two-DEA modules having opposite yaw torque bias directions are assembled into a four-DEA robot.



Extended Data Fig. 7 | Simulation of open-loop ascending flight and comparison with experimental results. **a**, Coordinate system definition of the four-wing robot model. Scale bar represents 1 cm. **b**, Top view schematic of the four-wing robot. l_x and l_y denote the distance from the robot's centre of mass to each wing's centre of pressure. **c**, Comparison of measured and simulated yaw (ψ) motion. The robot makes 11 revolutions with respect to its z axis 0.8 s after takeoff. **d**, Comparison of measured and simulated yaw rate ($\dot{\psi}$). The steady-state angular velocity of the robot's yaw rate is 17.5 revolutions per second. **e**, Simulated pitch (ϕ) and roll (θ) motion. Our simulation predicts that the steady-state oscillation with respect to the robot's X and Y axes is smaller than 3°. **f**, Simulation results of the robot's displacement after takeoff. The experimental measurement of the robot's vertical motion is superimposed on

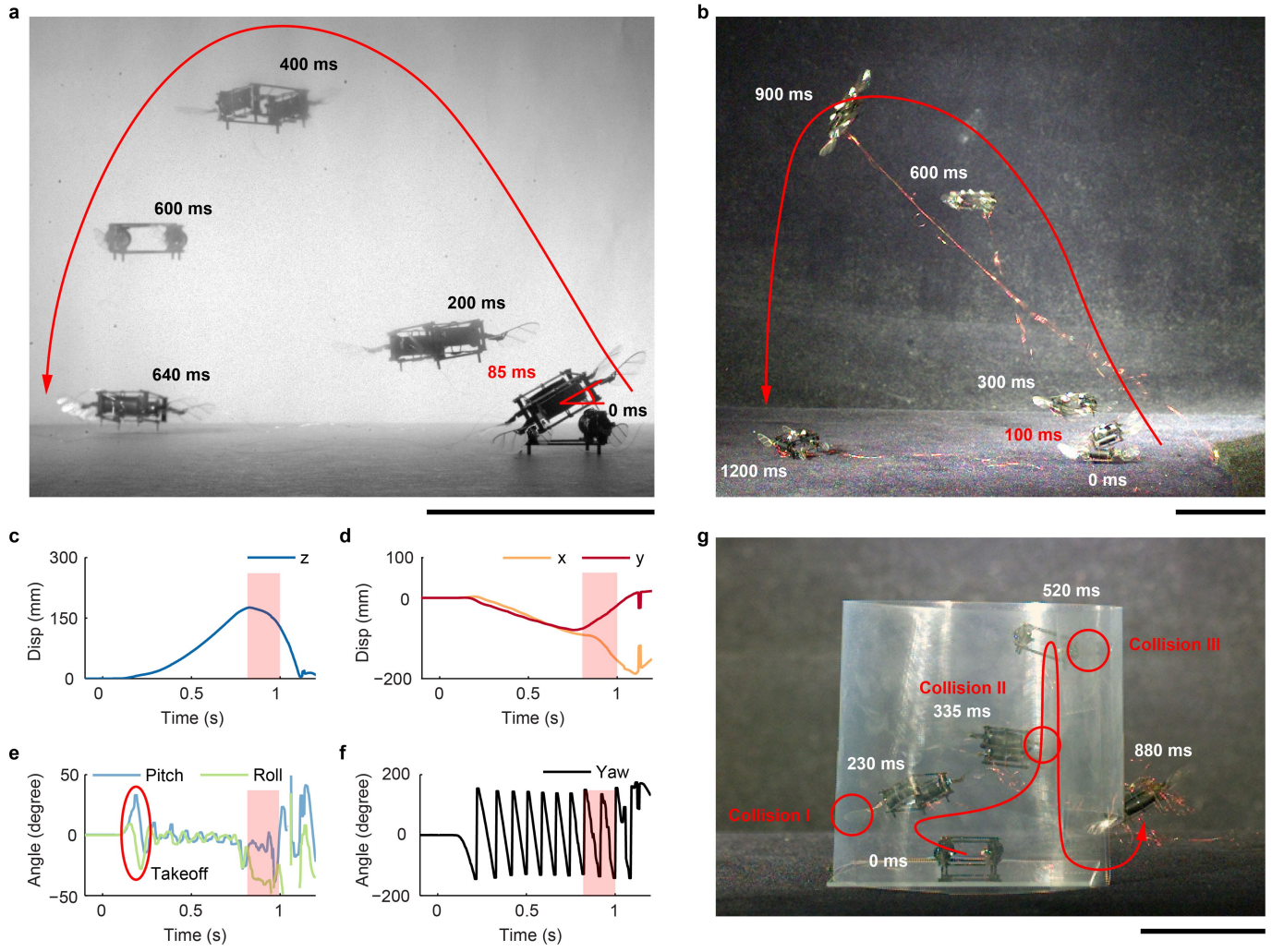
the same graph. The data shown in **c-f** correspond to the simulation and experiment shown in Supplementary Video 5 and Fig. 4b, c. **g-o**, Dynamical simulation of robot takeoff flights under different values of body yaw torque. **g**, Robot altitude as a function of time. **h**, A zoomed-in plot of robot altitude shortly after takeoff. This plot corresponds to the red region in **g**. **i**, Robot altitude at one second after takeoff as a function of input body yaw torque. **j**, Robot pitch motion as a function of time. **k**, A zoomed-in plot of robot pitch that corresponds to the red region in **j**. **l**, Maximum robot pitch deviation as a function of input yaw torque. **m**, Robot roll motion as a function of time. **n**, A zoomed-in plot of robot roll that corresponds to the red region in **m**. **o**, Maximum robot roll deviation as a function of input yaw torque.

Article



Extended Data Fig. 8 | Three passively stable ascending flights of a robot with two DEAs. **a–c**, Composite images of three one-second, open-loop ascending flights. **d–g**, Tracked robot altitude (**d**), x and y centre-of-mass position (**e**), pitch and roll orientation (**f**) and yaw rotation (**g**). The data shown

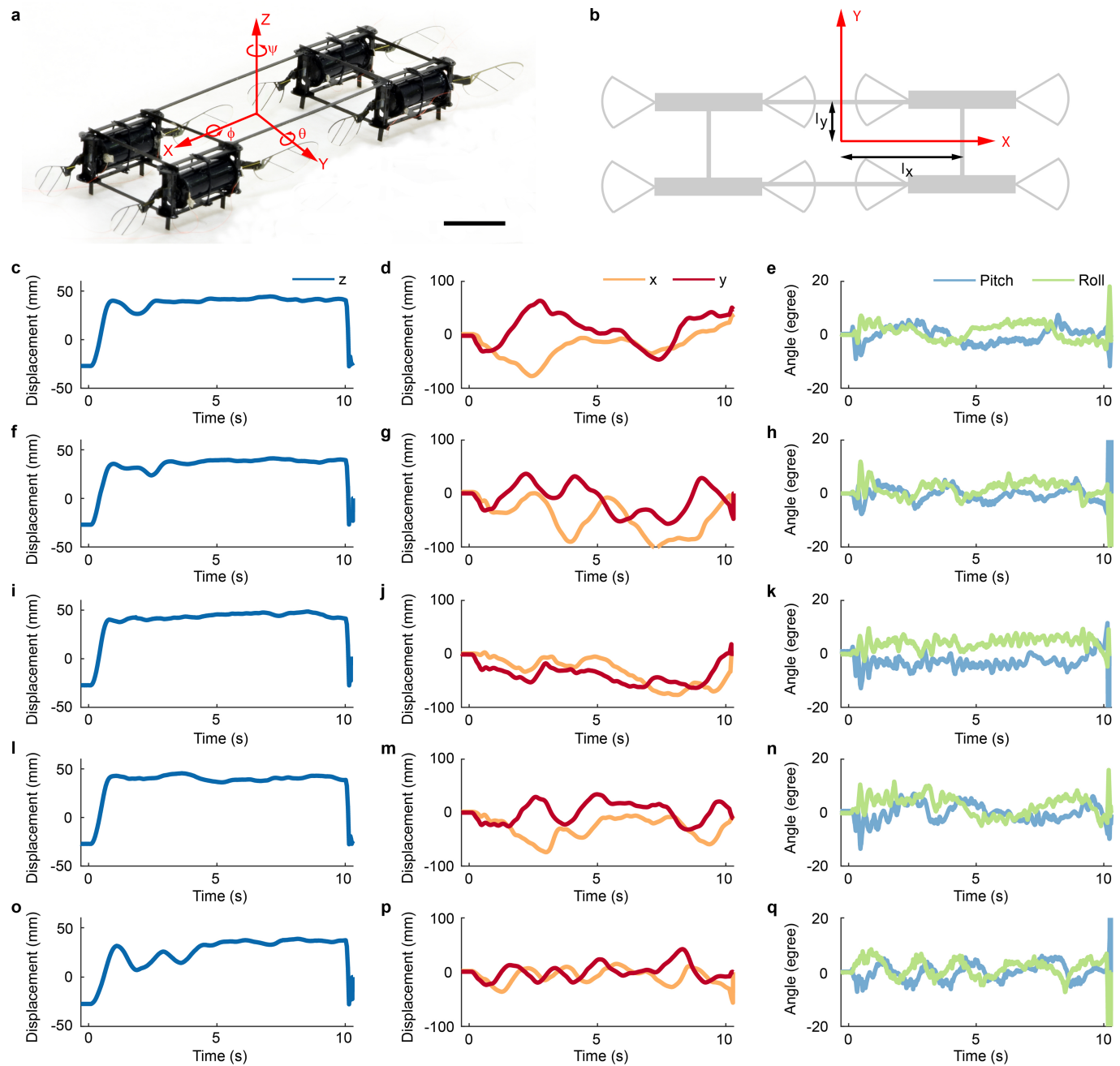
in **d–g** correspond to the flight shown in **a**. Similarly, **h–k** and **l–o** show the tracked flight data corresponding to the flights shown in **b** and **c**, respectively. Sudden jumps in the tracking data (**h**, **i**, **l** and **m**) indicate the time at which the Vicon motion capture system loses tracking. Scale bars in **a–c** represent 5 cm.



Extended Data Fig. 9 | Robot unbalanced takeoff flights and a failed collision recovery experiment. **a**, A composite image of a 0.5-s open-loop takeoff flight captured at 3,000 frames per second. The robot pitch deviation is approximately 35° at 85 ms after takeoff. **b**, A composite image of a 1-s open-loop takeoff flight conducted in the Vicon motion tracking arena. **c–f**, Tracked robot altitude (**c**), *x* and *y* centre-of-mass position (**d**), pitch and roll orientation (**e**), and yaw rotation (**f**). The data shown in **c–f** correspond to the flight in **b**. The red circle in **e** illustrates the large robot pitch and roll deviation after takeoff. The red-shaded regions in **c–f** show the changes of robot position and orientation after it is pulled by its tether. **g**, An example of a failed collision recovery experiment. The robot is destabilized after making the third collision. Scale bars in **a**, **b**, and **g** represent 5 cm.

(e), and yaw rotation (f). The data shown in c–f correspond to the flight in b. The red circle in e illustrates the large robot pitch and roll deviation after takeoff. The red-shaded regions in c–f show the changes of robot position and orientation after it is pulled by its tether. g, An example of a failed collision recovery experiment. The robot is destabilized after making the third collision. Scale bars in a, b, and g represent 5 cm.

Article



Extended Data Fig. 10 | Controller design of the eight-wing robot and hovering flight repeatability. **a**, Perspective view of the eight-wing robot with a superimposed coordinate system. The pitch (ϕ), roll (θ), and yaw (ψ) angles are defined with respect to the fixed X , Y and Z axes. Scale bar represents 1 cm. **b**, Top view schematic of the eight-wing robot. l_x and l_y denote the distance from the robot centre of mass to the geometric centre of each DEA. **c–q**, Tracked robot position (displacement relative to the origin of the Vicon motion

tracking system's coordinate system) and attitude data of five 10-s hovering flights. In these flights, we do not control the robot's yaw motion. **c, f, i, l, o**, The first column shows the robot's altitude as a function of time. **d, g, j, m, p**, The second column shows the robot's lateral position as a function of time. **e, h, k, n, q**, The last column shows the robot's pitch (ϕ) and roll (θ) motion as a function of time.

Extended Data Table 1 | Parameters for the conceptual design of the two-wing robot

Parameter	Symbol	Value
Robot mass	m	160 mg
Mean drag coefficient	$\overline{C_D}$	1.6
Mean lift coefficient	$\overline{C_L}$	0.7
Transmission ratio	T	2530 rad·m ⁻¹
Maximum lift to weight ratio	f_m	1.2
Robot transmission dimensions	t, w, l	25 μm, 1.2 mm, 200 μm
Young's modulus of polyimide film	E	2.5 GPa
Wing aspect ratio	AR	3
Wing span	R	9.9 mm
Wing span wise moment of inertia	I_{zz}	15 mg·mm ²
Wing span wise center of pressure	r_{cp}	7 mm
Air density	ρ	1.2 kg·m ⁻³
Wing hinge geometry	t_h, w_h, l_h	7.5 μm, 2.65 mm, 110 μm
DEA mass	m_a	100 mg
DEA natural resonance frequency	f_{res}	465 Hz
Heat generated during operation	Q	0.25 J·s ⁻¹
DEA heat capacity	C	0.15 J·K ⁻¹
Ambient temperature	T_a	28.7 °C
Initial temperature at onset of cooling	T_i	70 °C
Heat conduction rate during heating	K_1	0.04 s ⁻¹
Heat conduction rate during cooling	K_2	0.022 s ⁻¹

Article

Extended Data Table 2 | Physical and simulation parameters for the four-wing robot

Parameter	Symbol	Value
Mass	m	320 mg
Principal moment of inertia	I_{xx}, I_{yy}, I_{zz}	$2.99 \times 10^4, 2.41 \times 10^3,$ $3.13 \times 10^4 \text{ mg} \cdot \text{mm}^2$
Distance to robot center of mass	l_x, l_y	13.3, 7 mm
Lift force of each wing	$F_{L1}, F_{L2}, F_{L3}, F_{L4}$	0.86, 0.81, 0.82, 0.88 mN
Drag force of each wing	$F_{D1}, F_{D2}, F_{D3}, F_{D4}$	0.29, 0.29, 0.29, 0.29 mN
Body damping force coefficient	b_f	$0.5 \text{ mg} \cdot \text{mm}^{-1}$
Body damping torque coefficient	b_t	$1.5 \times 10^3 \text{ mg} \cdot \text{mm}^2$

These parameter values correspond to the simulation results shown in Extended Data Fig. 7.

Extended Data Table 3 | Values of flight controller parameters for hovering flights

#	Flight duration (s)	λ_0 (s ⁻⁴)	λ_1 (s ⁻³)	λ_2 (s ⁻²)	λ_3 (s ⁻¹)	A_0 (s ⁻²)	A_1 (s ⁻¹)	α (V/mN)	β (V)	$\gamma_1, \gamma_2, \gamma_3, \gamma_4$ (V)
1	10	13608	6631	798	62	25	125	82	1172	38, 80, 69, 34
2	10	13608	6631	798	62	25	125	82	1172	38, 80, 69, 34
3	10	27216	9946	570	57	25	125	82	1172	38, 80, 69, 34
4	10	30618	9946	570	57	25	125	82	1172	38, 80, 69, 34
5	10	54432	13262	713	71	25	125	82	1172	38, 80, 69, 34
6	16	54432	13262	713	71	30	150	82	1172	38, 85, 74, 34

These values correspond to the flights shown in Fig. 4e–i and Extended Data Fig. 10.